

Fall 2014

## Reduction of Secondary Flow Losses in a Turbine for Use in Man-Portable Power Generation

Andrew J. Yatsko E.I.  
*Embry-Riddle Aeronautical University - Daytona Beach*

Follow this and additional works at: <https://commons.erau.edu/edt>



Part of the [Aerospace Engineering Commons](#)

---

### Scholarly Commons Citation

Yatsko E.I., Andrew J., "Reduction of Secondary Flow Losses in a Turbine for Use in Man-Portable Power Generation" (2014). *Dissertations and Theses*. 190.  
<https://commons.erau.edu/edt/190>

This Thesis - Open Access is brought to you for free and open access by Scholarly Commons. It has been accepted for inclusion in Dissertations and Theses by an authorized administrator of Scholarly Commons. For more information, please contact [commons@erau.edu](mailto:commons@erau.edu).

REDUCTION OF SECONDARY FLOW LOSSES IN A TURBINE FOR USE IN MAN-  
PORTABLE POWER GENERATION

By

Andrew J. Yatsko E.I.

A Thesis Submitted to the Graduate Studies Office in Partial Fulfillment of the  
Requirements for the Degree of Master of Science in Aerospace Engineering

Embry-Riddle Aeronautical University

Daytona Beach, FL

Fall 2014

**Reduction of Secondary Flow Losses in a Turbine for Use in Man-Portable Power  
Generation**

By Andrew J. Yatsko E.I.

This thesis was prepared under the direction of the candidate's thesis committee chair, Dr. Magdy S. Attia, Department of Aerospace Engineering, and has been approved by the members of his thesis committee. It was submitted to the Aerospace Engineering Department and was accepted in partial fulfilment of the requirements for the degree of Master of Science in Aerospace Engineering

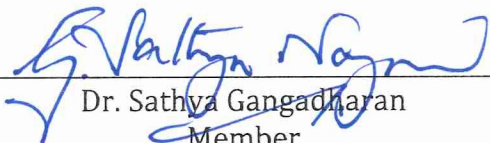
THESIS COMMITTEE



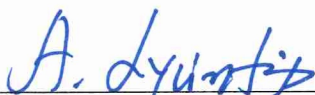
Dr. Magdy Attia  
Chairman



Dr. Mark Ricklick  
Member



Dr. Sathya Gangadharan  
Member



Dr. Tasos Lyrintzis, Department Chair



Dr. Robert Oxley, Associate Provost

## **Acknowledgements**

I would like to thank my advisor Dr. Magdy Attia for all of his support, guidance and education provided through our interactions. Additionally I would like to extend my gratitude to Dr. Mark Ricklick and Dr. Sathya Gangadharan for their assistance and support of my work through my graduate career. I would like to thank my wife, Erin, for all of her support and comfort through the research and time away from home to make my career a reality. A sincere amount of gratitude towards Mr. George Minkkinen, Teledyne Turbine Engines, Principle Turbine Design Engineer (ret.), for his help learning turbine design methodology and parameters inside and out. I would also like to thank the management team at Teledyne Turbine Engines, specifically, Mike Rudy, VP & General Manager, and Dale Jessick, VP Advanced Development, for allowing me to use the company's Aero-Turbine analysis tools after hours to complete the bulk of my analysis. Last but not least I would like to thank Robert "Bob" Van Newhouse, Teledyne Turbine Engines, Senior Design Engineer, for all of his help learning the Unigraphics software and how to accurately apply it to the design of turbine cascades. None of the work would have been possible without the support of the aforementioned.

## **Abstract**

**Author:** Andrew J. Yatsko E.I.

**Title:** Reduction of Secondary Flow Losses in a Turbine for Use in Man-Portable Power Generation

**Institution:** Embry-Riddle Aeronautical University, Daytona Beach Campus

**Degree:** Master of Science in Aerospace Engineering

**Year:** 2014

As the world has moved into a more energy-demanding environment, there has been the push for higher energy density in a smaller package. One of the potential solutions is through the application of a gas turbine engine; yet the challenge is extracting the energy efficiently through the small components. The focus of the research is on the turbine components and how the secondary flow losses from the generated airfoil shapes can be reduced to improve component performance. One of the secondary flow loss items to be addressed is the generation of the Horseshoe Vortex. The Horseshoe Vortex is an aerodynamic phenomenon that occurs in axial turbine cascades that degrades the aerodynamic performance. This research will show that through airfoil design optimization, the Horseshoe Vortex on small turbine nozzles can be reduced. The initial turbine design was generated using simple incompressible flow calculations and then run through a Navier-Stokes SST solver. This solver allows for the interaction of the boundary layer with the airfoil geometry, therefore generating a new set of inlet velocity triangles. The geometry was then optimized to match the new inlet velocity triangle. The new optimized

airfoil was run through the same boundary layer build up, and the same boundary conditions as the original incompressible design. The presented results will show that the Horseshoe Vortex has been mitigated and that the total pressure distribution at the exit of the turbine inlet nozzle cascade has improved by 7.6 %.

## Table of Contents

Acknowledgements.....	iii
Abstract.....	iv
List of Figures .....	vii
List of Tables .....	ix
Nomenclature.....	x
1. Problem Statement.....	1
2. Background and Theory .....	2
2.1 History of Portable Power Generation.....	2
2.2 Thermodynamic Cycles.....	3
2.2.1 Brayton Cycle .....	3
2.2.2 Brayton cycle efficiency .....	4
2.2.3 Recuperated Brayton Cycle .....	6
2.3 Turbine Aerodynamic Characteristics .....	7
2.4 Horseshoe Vortex.....	9
3. Design Methodology.....	16
4. Problem Setup .....	18
4.1 Portable Power Generation Design Parameters for 10kW system .....	18
4.2 Meanline Analysis .....	20
4.3 Airfoil Generation and Blade Stack-up.....	21
4.4 Meshing Geometry and Computational Fluid Dynamics (CFD).....	23
5. Results .....	28
5.1 Comparison of Meanline to CFD .....	28
5.2 Geometry modification for optimization, Original Geometry .....	32
5.2.1 Geometry Optimization .....	34
6. Summary.....	40
7. Future Work / Recommendations.....	44
8. References.....	45
9. Appendix A: NPSS model output .....	48

## List of Figures

Figure 1: Ragone Plot of some available fuels [1] .....	2
Figure 2: Ideal Brayton Cycle T-s diagram [6] .....	4
Figure 3: Simple Brayton Cycle, 1800F Turbine Inlet Temperature, showing a variety of compressor/turbine efficiencies [7] .....	5
Figure 4: Recuperated Cycle, 80% Compressor and Turbine Efficiencies, 1800F Turbine Rotor Inlet Temperature, Varying Recuperator Effectiveness [7] .....	6
Figure 5: Brayton cycle with Regenerator (left), Ideal Regenerated Brayton cycle T-s diagram (right) [5] .....	6
Figure 6: Breakdown of principle turbine losses [10] .....	8
Figure 7: Types of Cascade Flow Losses [10] .....	9
Figure 8: Horseshoe Vortex Formation with Stagnation Region [11] .....	10
Figure 9: Full Horseshoe Vortex formation in a Turbine Cascade [12] .....	11
Figure 10: Suction Side (Passage) Vortex sheet [10] .....	12
Figure 11: Unsuccessful profile fillet (a), Final Fillet design (b). (13) .....	13
Figure 12: Zess et al. CFD results of filleted vane (13) .....	13
Figure 13: Schematic of filled geometric design parameters. (14) .....	14
Figure 14: Original Fillet Design (top), Optimized Fillet Design for reduced wall temperatures (bottom) (14) .....	15
Figure 15: Comparison of Original Fillet Design (top) wall temperatures to the Optimized Fillet (top) (15) .....	15
Figure 16: Clearance losses increase as engine size decreases [16] .....	21
Figure 17: Barrel Sections of Cascade Stacked about the centroid .....	22
Figure 18: ANSYS Workbench Fluid Flow Project Schematic .....	23
Figure 19: Mesh setup Details Original Turbine Cascade .....	24
Figure 20: Swept Mesh of Original Turbine Cascade .....	25
Figure 21: Total Temperature Inlet Gradient .....	27
Figure 22: Total Pressure Inlet Gradient .....	27
Figure 23: Meridional View of Static Pressure distribution at 0.5 span .....	29
Figure 24: Velocity streamlines indicating the Saddle Point .....	30
Figure 25: Velocity Vector plot at the region of interest, full cascade span .....	30
Figure 26: Velocity vector plot at the region of interest, hub region .....	31
Figure 27: Comparison of Original CFD Total Pressure distribution to meanline ....	31
Figure 28: Comparison of the Original CFD Total Temperature distribution to meanline .....	32
Figure 29: Absolute Flow angle vs. Normalized Span for Original CFD .....	33
Figure 30: Optimized Cascade Geometry Stack Up .....	34
Figure 31: Final Optimized Geometry showing mesh of Leading edge fillet .....	35
Figure 32: Top view of mesh for Final Optimized Geometry .....	36
Figure 33: Optimized Geometry showing HSV with Streamline and Vector plots. ....	37
Figure 34: Optimized Geometry showing weak HSV .....	37
Figure 35: Optimized Geometry vector plot showing flow moving down passage rather than recirculating .....	38
Figure 36: Inlet Total Pressure vs. Normalized span for Optimized Geometry and Meanline .....	39

Figure 37: Inlet Static Pressure vs. Normalized span for Optimized Geometry and Meanline .....	39
Figure 38: Inlet Total Temperature vs. Normalized span for Optimized Geometry and Meanline .....	40
Figure 39: Inlet Static Pressure vs. Normalized Span for all CFD and Meanline .....	41
Figure 40: Inlet Total Pressure vs. Normalized Span for all CFD and Meanline .....	41
Figure 41: Inlet Total Temperature vs. Normalized Span for all CFD and Meanline .....	42
Figure 42: Exit Total Pressure vs. Normalized Span for CFD .....	43
Figure 43: Exit Total Temperature vs. Normalized Span for CFD .....	43

## List of Tables

Table 1: Thermodynamic Cycle Requirements from Table 1 in WASIC paper [7] .....	18
Table 2: NPSS Heat Exchanger initial inputs .....	19
Table 3: Assumptions for NPSS model of 10kW System from Table 1 .....	19
Table 4: NPSS Model Cycle and Turbine Output .....	20
Table 5: Turbine Stage Meanline Nozzle Exit Pressure and Temperature Conditions .....	21
Table 6: CFD Inlet Boundary Gradient Setup .....	28

## Nomenclature

$\alpha$	Absolute Flow Angle	Degrees
$V_{axial}$	Axial Flow Velocity	ft/s
$V_{circumferential}$	Circumferential Flow Velocity	ft/s
$\eta_{TH}$	Thermal Efficiency	%
LHV	Lower Heating Value	Btu/lb <sub>m</sub>

## **1. Problem Statement**

As the turbomachinery components get small enough to fall into the man-portable category, it becomes difficult to maintain high component efficiencies. The inefficiency is due mainly to losses that are sometimes negligible for large gas turbine engines. These losses, such as tip clearance losses, mixing losses, and other secondary flow losses, start to become major players and, in some size ranges, can become the dominant factor for component losses. It is the objective of this research to reduce these losses as much as possible focusing on the secondary flow regime. One main area of improvement is what is known as the cross-passage vortex or Horseshoe vortex. This objective will be approached by recreating a cycle model found in literature, generating a potential turbine stage in an in-house meanline code, and then running the design through Computational Fluid Dynamics (CFD). Through analyzing the effects of the boundary layer, from the CFD, on the original blade profile and inlet velocity triangles it will be shown that the secondary flow losses and Horseshoe Vortex can be reduced through geometry optimization.

## 2. Background and Theory

### 2.1 History of Portable Power Generation

As the world becomes more technology dependent there is the need to supply more power for the gadgets used. Sticking to the current method of power generation for these technology systems, batteries, the weight would soon outweigh the benefits of the system. The systems would no longer be easily contained or would require large heavy power packs for extended use. As technology has progressed there is a viable solution in the realm of lithium-polymer batteries as well as fuel cells, but when looking at the energy content of these systems as it stands today they are still dwarfed by systems employing hydrocarbon fuels, Figure 1. This leads to the problem statement at hand: how can power generation be both light weight and run for extended periods of time?

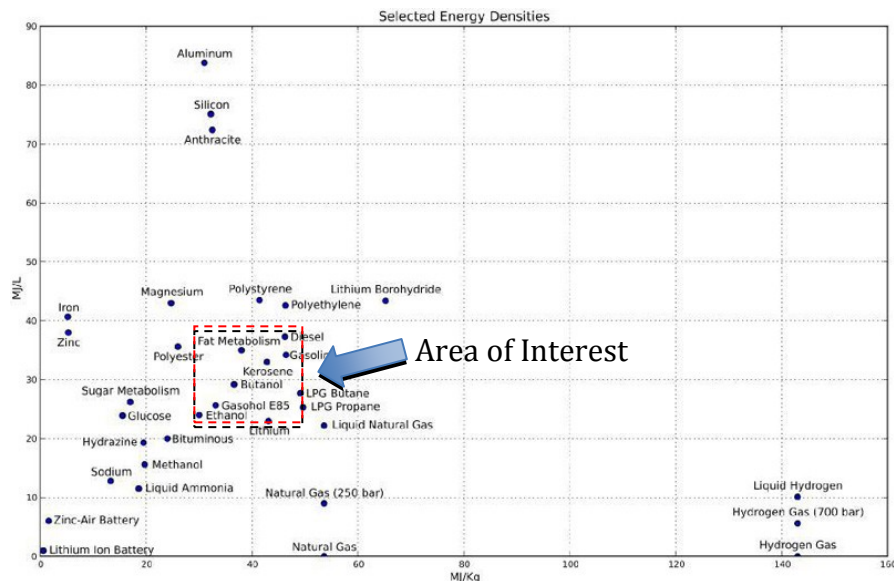


Figure 1: Ragone Plot of some available fuels [1]

The Ragone plot shows Energy Density (Mj/L), the amount of energy available for a given volume, versus Specific energy (Mj/kg), the amount of energy per unit mass. To sum this up, the farther up the y-axis one travels, the less fuel volume is required to do the same amount of work, and the farther to the right one moves on the x-axis the lighter the fuel weight will be.

There are many solutions of portable efficient power generation available on the market today. This can be seen in batteries (Energizer, Duracell, etc.), portable generators (Honda, John Deere, etc.), and advances into the small turbomachinery market (Capstone Turbine Corporation). Each of the aforementioned technologies has its respective place, but for a trade-off in either power or weight. When compared on a size scale a nine volt battery weighs in around 1.6oz and can produce approximately five watts per hour (2), whereas the standard home generator weighs 262lb and at the rated load burns 5.27lb of gasoline per hour producing around 7kW of power (3) for as long as there is fuel supplied. Where a 30kW system running at 25% electrical efficiency that is currently available and ready to connect for power weighs in around 891lb for the system, this includes electronics weight (4). This turbomachinery system is a ground system and is built for durability, not portability, which is why it weighs in more than three times the weight of a commercial off the shelf portable generator.

## **2.2 Thermodynamic Cycles**

### **2.2.1 Brayton Cycle**

There are many types of thermodynamic cycles, such as power, refrigeration, and heat pump. A thermodynamic cycle is defined as, "A sequence of processes that

begins and ends at the same state.”(5) The main focus will be on the power cycle for the gas turbine engine, the Brayton cycle, Figure 2.

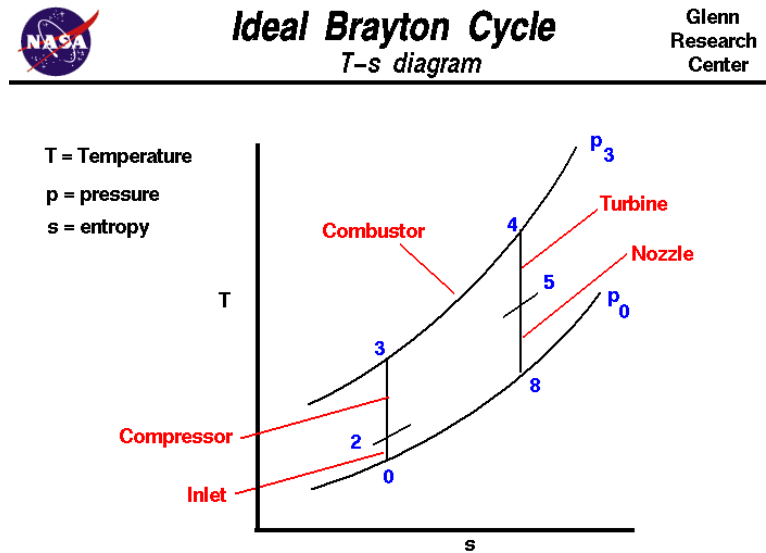


Figure 2: Ideal Brayton Cycle T-s diagram [6]

The Mollier Diagram is an enthalpy (or sometimes, temperature) versus entropy plot, Figure 2. The air is compressed moving from station 2 to station 3 via isentropic compression, then the air is heated from station 3 to station 4, where the available work is extracted from station 4 to station 5 via isentropic expansion. The methodology behind the Brayton cycle is to combust the air in an isobaric process. Then, as the volume is allowed to expand and moves down stream to the turbine, excess work can be extracted to power the compressor, with any remaining energy left over for the nozzle to create thrust. Due to the cycle being a power generation cycle all available work will be extracted through the turbine and having almost zero net thrust from the system.

### 2.2.2 Brayton cycle efficiency

The efficiency of a Brayton cycle is calculated as work output over heat input.

$$\eta_{TH} = \frac{\text{Energy Output (hp)} * 0.706787 \left( \frac{\left( \frac{Btu}{s} \right)}{hp} \right)}{\text{Heat Input} \left( \frac{Btu}{s} \right)} * 100$$

**Equation 1: Cycle Thermal Efficiency**

Where;

$$\text{Heat input} = LHV \left( \frac{BTU}{lbm} \right) * \text{Fuel Flow} \left( \frac{lbm}{s} \right)$$

**Equation 2: Heat Input equation**

To obtain a perfect cycle it would require extracting just as much energy out of the system as put into the system. Since this is not possible, due to the 2<sup>nd</sup> Law of Thermodynamics, the thermal efficiency of most non-recuperated gas turbine engines, in the low Overall Pressure Ratio (OPR), less than four OPR for our area of interest, will fall into the range of 15-25% for a non-recuperated cycle, Figure 3.

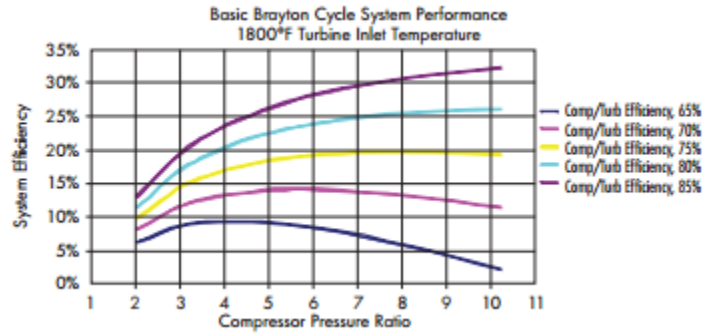


**Figure 3: Simple Brayton Cycle, 1800F Turbine Inlet Temperature, showing a variety of compressor/turbine efficiencies [7]**

If the cycle is recuperated, the thermal efficiency can get on the order of 27-37%, with some occasional outliers due to technology advancements, Figure 4. This efficiency improvement comes by making the denominator “Heat Input” smaller by using less fuel to add the same amount of heat to the air.

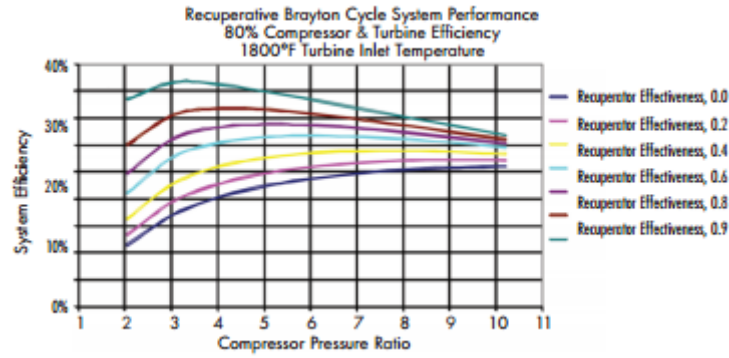


Figure 4: Recuperated Cycle, 80% Compressor and Turbine Efficiencies, 1800F Turbine Rotor Inlet Temperature, Varying Recuperator Effectiveness [7]

### 2.2.3 Recuperated Brayton Cycle

The Brayton cycle with a recuperator can be seen in Figure 5, where the difference is pre-heating the air, with waste exhaust heat, after it leaves the compressor and before it goes into the combustor.

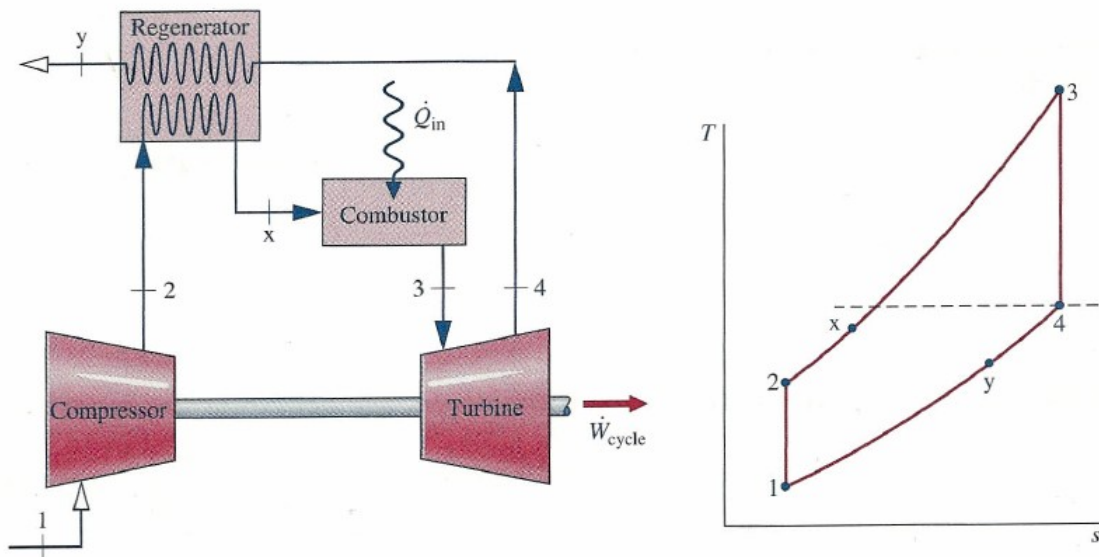


Figure 5: Brayton cycle with Regenerator (left), Ideal Regenerated Brayton cycle T-s diagram (right) [5]

This preheat allows the temperature of the air to rise without burning additional fuel. This process is similar to the original Brayton cycle. The air is compressed moving from station 1 to station 2, then the air is heated from station 2 to station x

from the turbine exhaust gas, fuel is added and combusted from station x to station 3, the available work is extracted from station 3 to station 4, then heat is removed from station 4 to station y which heats the air from station 2 to station x. This means the air is only being heated from station x to station 3 where as in the traditional Brayton cycle the air must be heated from station 2 to station 3, thus requiring less fuel in a recuperated cycle to heat the same amount of air. In turn this allows the cycle efficiency to increase by a significant percentage as a consequence of reduced fuel consumption, but as is taught, "There is no free lunch." Recuperators also known as regenerators are heat exchangers. The effectiveness of a heat exchanger is based on material properties, and heat transfer coefficients, but the driving factor is surface area, and increased surface area is usually associated with more volume of material, which is weight. Some of the smallest recuperators run between 80% to 90% effectiveness and still weight a significant amount compared to the engine weight (8). For an example one can look at the AGT 1500 turboshaft developed by Lycoming for the Abrams Tank family. The Recuperator was as big as the turbomachinery and was made of steel, and weighed an estimated 25% of the 2500lb system weight (9).

### **2.3 Turbine Aerodynamic Characteristics**

The engine cycle being considered is strictly for power generation, compared to the typical thrust engine, the desired turbine characteristics are going to be more relaxed. The main area that can be relaxed can be seen in the turbine exhaust; where in a typical thrust engine it is ideal for the flow leaving the last turbine stage to have no swirl, in power generation removing all of the residual swirl may not be

necessary. This excess swirl is typically a byproduct of high work turbines; it also may help create extra turbulence inside the recuperator for additional heat transfer, which is desirable. A typical turbine stage is designed to remove only enough energy from the flow to power the compression system and any necessary power generation through an alternator/generator. No system can perfectly add or remove energy to or from a system without losses. While minimizing the losses is the name of the game, there are some losses that are always going to be present, such as tip clearance, profile losses, and mixing losses to name a few. As the turbine stage has flow passed through it, it is subject to different losses adding up to a total loss coefficient. The smaller the total loss coefficient, the more efficient the component can become. Some of the losses that affect turbine cascades can be seen in Figure 6.

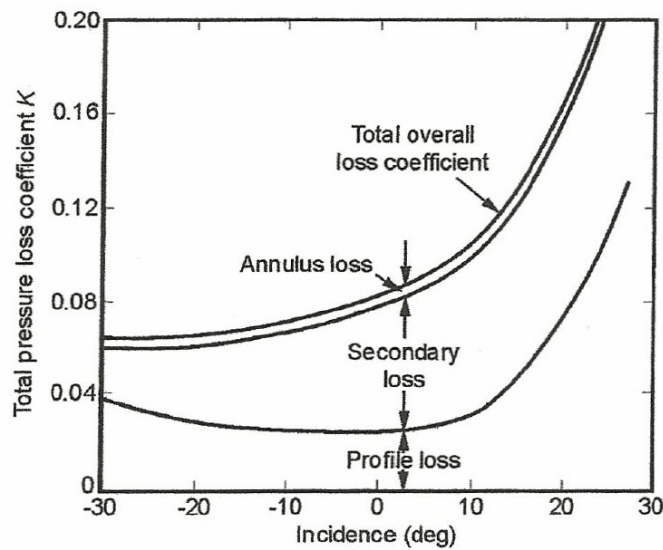
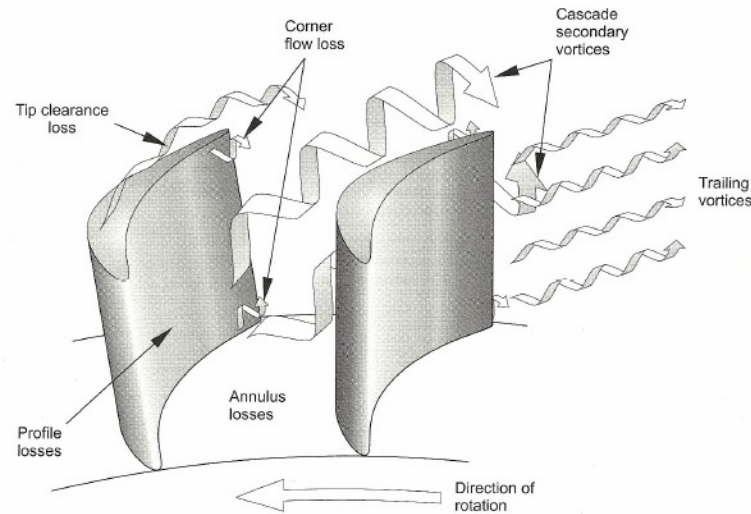


Figure 6: Breakdown of principle turbine losses [10]

Notice that the secondary flow losses can make up almost 75% of the total losses of a turbine cascade for near zero incidence angles. The profile loss is due to skin friction on the blade surface, and annulus loss due to friction on the endwall

surfaces (10). This large percentage in the secondary flow regime is where many engineers spend their careers trying to make gains in performance. Some of the types of cascade flow losses can be seen in Figure 7.



**Figure 7: Types of Cascade Flow Losses [10]**

By reducing any one of the aforementioned types of losses the performance of the cascade can be increased. One of the areas in the secondary flow region, where gains can be made, is in the reduction of the cross-passage flow vortex, which is initiated by what is known as the horseshoe vortex.

## **2.4 Horseshoe Vortex**

The horseshoe vortex (HSV) is a type of secondary flow phenomenon in turbine cascade leading to a cross-passage vortex. The HSV is formed from the interaction of a three dimensional boundary layer with the cascade end wall. As shown in Figure 8, as the flow approaches the cascade, the velocity profiles due to the boundary layer start to become skewed and the flow forms a surface of separation. This separation starts to occur at some distance,  $S$ , from the cascade in the stagnation

region. “In the neighborhood of this separation region, the flow develops a separated vortex sheet which curls up around the cylinder at its base like a horseshoe” Schlichting (11).

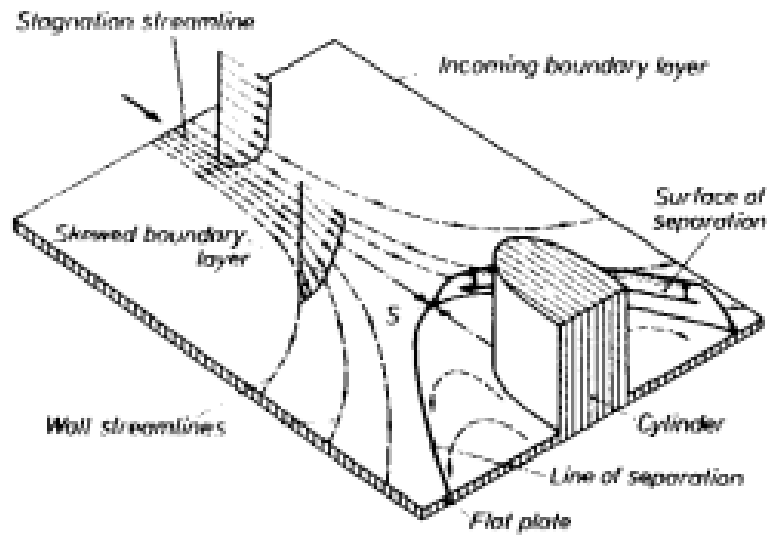
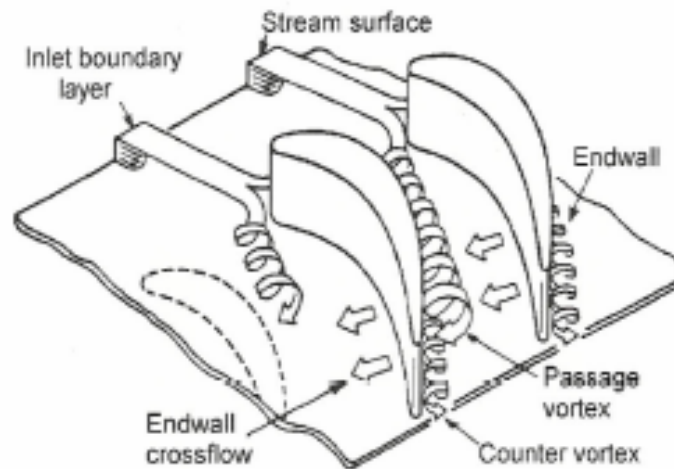


Figure 8: Horseshoe Vortex Formation with Stagnation Region [11]

As the HSV begins to generate the pressure surface vortex is dragged across the passage due to its pressure gradient, where it then mixes with the suction surface vortex, Figure 9. This latter vortex is known as the cross-passage vortex and is equally, if not more, guilty of decreasing cascade performance.



**Figure 9: Full Horseshoe Vortex formation in a Turbine Cascade [12]**

The suction surface vortex, when originally generated, starts slightly differently due to a laminar separation bubble. This was first described by Klein (1966) and later by Langston et al. (1977) in a similar model, Figure 10. Notice Klein's description of the laminar separation bubble. This usually occurs near the throat of the cascade; in this context due to residual acceleration, the flow reattaches shortly after separation (10).

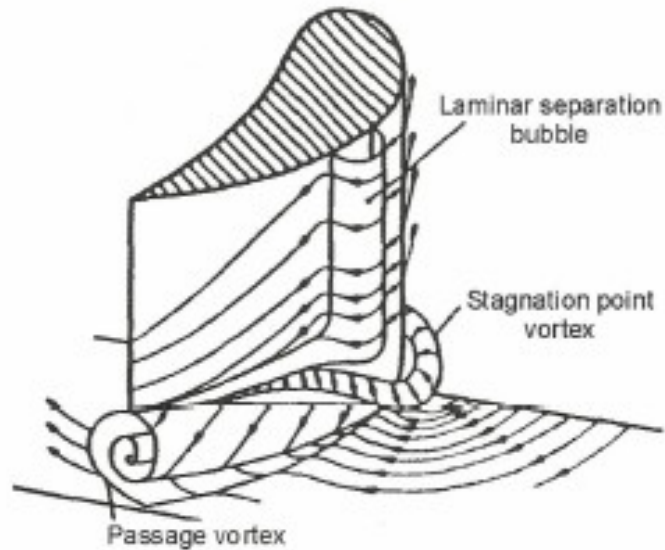


**Figure 10: Suction Side (Passage) Vortex sheet [10]**

There have been previous studies with the goal of directly minimizing the horseshoe vortex and the secondary flow losses associated with the vortex generation. This included work by Zess et al. (13) on the introduction of a leading edge fillet. Zess et al. used variations from prior research to find an effective way to mitigate the HSV, Figure 11. The fillet that worked the best was that of one boundary layer high and two boundary layers in length, and it was symmetric about the stagnation line. The results from their study can be seen in Figure 12.

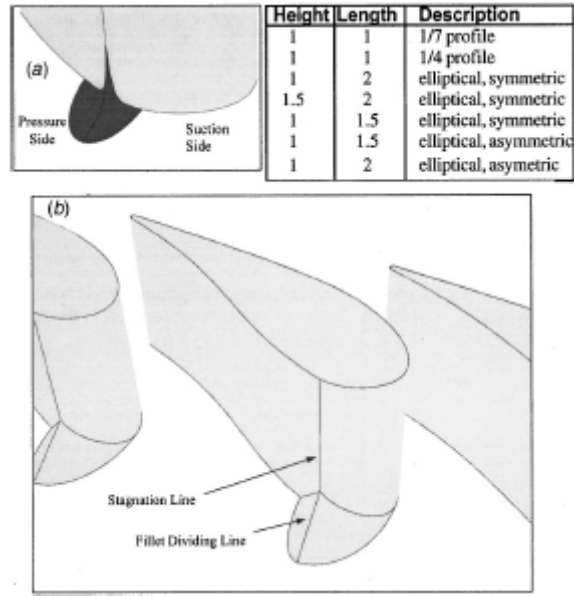


Figure 11: Unsuccessful profile fillet (a), Final Fillet design (b). (13)

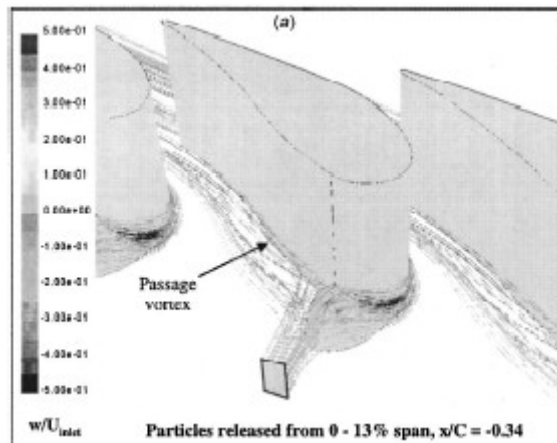
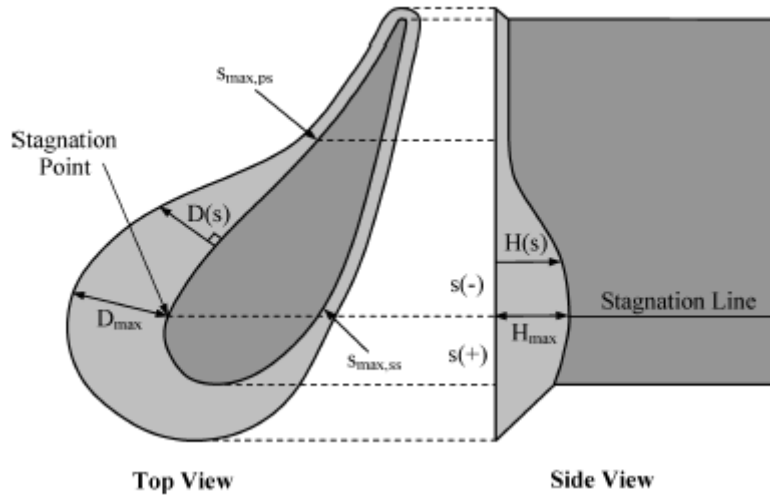


Figure 12: Zess et al. CFD results of filleted vane (13)

Additional work was done by Lethander et al. (14) on end wall junction optimization where parameters were set, Figure 13, and varied to obtain a set reduction in wall temperature.



**Figure 13: Schematic of filled geometric design parameters. (14)**

From these variables there were 64 design simulations performed, and the final design was selected. The design shows roughly the same results as Zess et al. (13), that the length of the fillet ( $D_{max}$ ) must be greater than the height of the fillet ( $H_{max}$ ). When this optimization was performed, the streamline patterns can be seen to have a more uniform flow around the cascade, Figure 14. There was also the realization that the amount of surface area needing to be cooled was less due to the temperature reduction at the end wall, owing to the reduction of the HSV, Figure 15.

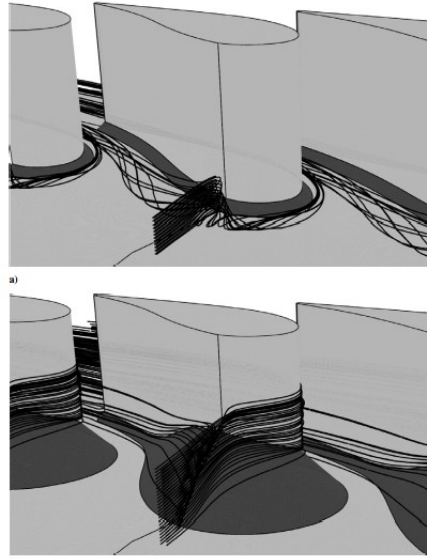


Figure 14: Original Fillet Design (top), Optimized Fillet Design for reduced wall temperatures (bottom)  
(14)

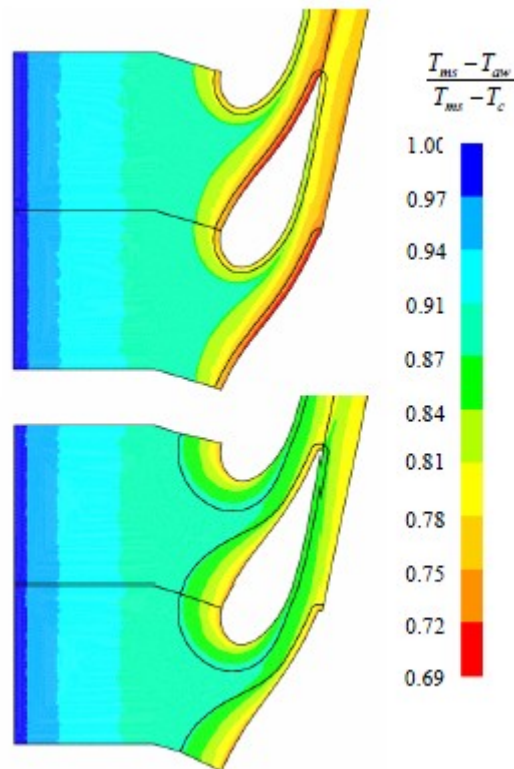


Figure 15: Comparison of Original Fillet Design (top) wall temperatures to the Optimized Fillet (top)  
(15)

### **3. Design Methodology**

There are many methods to approach the design of a turbine stage. The main item to have is the design requirements. Once the requirements are established, this sets the stage for how to proceed on the turbine selection and design. This leads to the following questions, does a turbine exist that will meet the requirements, does an existing industry turbine need to be refined to meet the efficiency goals, or does a turbine need to be a clean sheet turbine. Once this is decided, the first stop in the design process is a 1-D meanline level analysis. It is at this point that the imperial loss models are implemented, adding a level of real world design and test experience. The loss models take into account items including tip losses, mixing losses, pumping losses for cooling passages, blade incidence and deviation losses to name a few. All of this is done based on some basic input parameters and usually at the meanline. Meanline analysis is slowly growing to incorporate the hub, mean and shroud of the component to become more of a reduced through flow code. Once the designer is satisfied with the 1-D code and it meets the desired requirements, it is now time to add a little more fidelity to the model. The streamline code or better known as a 2-D code does the meanline calculation at a specified number of streamlines that would span the component from hub to shroud. What is accounted for at this point along the design method is the radial equilibrium, the fact that as air rotates it has the ability to compress. So this means that the air at the shroud region of the blade acts differently than the air at the mean region and at the hub region. The viscosity of the air is usually still ignored through the streamline code. It is not until a full computational fluid dynamics (CFD) model is created, that the viscosity is

taken into account, but before this can be completed, a blade profile is required. Up to this point in time, a NACA primary or secondary airfoil would suffice for a turbine cascade, and many companies still rely on this methodology, but with the growing capability of Computer Aided Drafting (CAD) which has led to more experimentation with arbitrary airfoil shapes to better suit the requirements. The CAD modeling and manipulation can be some of the most strenuous work and will vary from user to user. For reference, many designers can generate the same blade profiles via meanline, and streamline, but it is the CAD which separates users apart. Once the CAD model is complete, it can be setup for meshing and then run in a Navier-Stokes (CFD) solver. The type of solver used can vary depending on the application, for most turbomachinery a solver along the lines of SST (Shear Stress Transport) for ANSYS CFX will do the job. The fidelity of the model comes down to the quality of the mesh, and the CFD setup. Once the model has been run successfully and deemed by the designer that the CFD solver has “converged”, an analysis of the model can be done and the model geometry can be changed as deemed necessary to further refine the design to meet the requirements.

## 4. Problem Setup

### 4.1 Portable Power Generation Design Parameters for 10kW system

The Design parameters for the turbine came from building the cycle found in the Cycle published in the Reference 7, in the Numerical Propulsions System Simulation (NPSS) software, Table 1.

**Table 1: Thermodynamic Cycle Requirements from Table 1 in WASIC paper [7]**

Inlet Airflow	650 lb/hr	Compressor Air Outlet Temperature	330°F
Fuel Input	5.06 lb/hr, No. 2 fuel	Recuperator Air outlet Temperature	1253°F
Compressor Inlet Pressure	14.7 psia	Turbine Outlet Temperature	1356°F
Compressor Discharge Pressure	44.1psia	Exhaust Gas Temperature	449°F
Pressure Loss across Combustor	1.5 psi	Operating Speed	110,000
Pressure Loss across Recuperator	1.0 psia	Compressor Impeller Diameter	3.1 inches
Compressor Air Inlet Temperature	70°F	Turbine Rotor Diameter	3.5 inches
Turbine Inlet Temperature	1800°F	Compressor Efficiency	75%
Regenerator Effectiveness	0.9	Turbine Efficiency	80%
Overall Mechanical / Electrical Efficiency	85%	Overall System Thermal Efficiency	37%

When the cycle was created, it in fact was providing a series of difficulties, due to how the heat exchanger element works in NPSS. An initial estimation of the pressures, temperatures and flow was required in order for the cycle to know where to start as it began the solver process. This in turn meant that a non-recuperated cycle model had to be generated. Then once the solver ran and provided the output of temperature, pressure, and flow it provided a reasonable estimate for the recuperated cycle model. The values used as the input can be seen in Table 2.

**Table 2: NPSS Heat Exchanger initial inputs**

Actual Flow	0.18462	lb <sub>m</sub> /s
Total Pressure	16.10802	psi
Total Temperature	1856.26870	R
Water to Air Ratio (WAR)	0.0	
Fuel to Air Ratio (FAR)	0.0	

After multiple attempts it was realized that the NPSS cycle model would not actually converge on the same turbine efficiency, cycle fuel flow, or cycle thermal efficiency as stated in the table, yet all of the temperatures and pressures would match to within 0.5% of the numerical value listed in Table 1. It should also be noted that the NPSS cycle model of Table 1, will need to have some assumptions made about it, Table 3.

**Table 3: Assumptions for NPSS model of 10kW System from Table 1**

Inlet Recovery Losses	1.0
Burner Efficiency	1.0
Duct losses	0.0
Nozzle Thrust Coefficient	1.0
Nozzle Discharge Coefficient	1.0

These assumptions are necessary since the fact that the engine is in an uninstalled environment. While these assumptions are not ideal, they were made so the cycle would converge. The Output from this NPSS model is provided in Appendix A, but the main parameters of notice are listed in Table 4.

**Table 4: NPSS Model Cycle and Turbine Output**

Total Fuel Burn	5.319	lb <sub>m</sub> /hr
Power Output	13.41	hp
BSFC (Brake Specific Fuel Consumption)	0.396	lb <sub>m</sub> /hr/hp
Cycle Thermal Efficiency	34.8	%
Turbine Inlet Corrected Flow	0.318	lb <sub>m</sub> /s
Turbine Efficiency	87	%
Turbine Corrected Work (DHRC)	27.55	Btu/lb <sub>m</sub>

The cycle efficiency is calculated via Equation 1 from section 2.2.2. Based on this it is possible to get the 10kW system, but some higher efficiency components are required.

## 4.2 Meanline Analysis

The cycle shows that an 80% adiabatic efficient turbine is required to achieve the desired 36.6% cycle thermal efficiency, Table 1. After running a one dimensional meanline turbine aero design code, which implements the Ainley and Mathison loss models, it shows that an efficiency of 84% is currently feasible. The main losses that are attributed to a turbine vanes and blades can be seen in Figure 7. This shows that for the standard turbine less than 10% of the losses come from annulus losses, and the majority of losses come from the secondary flow losses, which include mixing plane losses, Figure 6. (10). While the loss breakdown shown by Mustapha may hold true for conventionally sized turbine stages, it has been shown that, when the tip clearance becomes approximately 10% of the blade height it would be deemed to have a larger impact on the overall losses Figure 16.

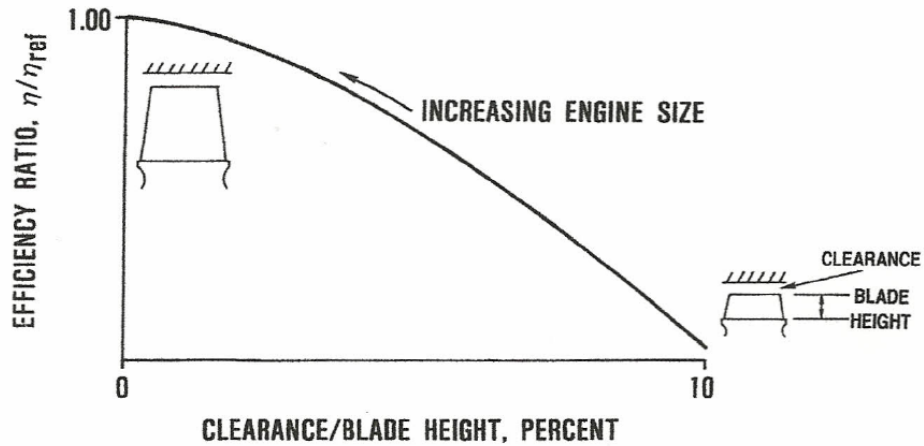


Figure 16: Clearance losses increase as engine size decreases [16]

One other item of concern is the increase of the drag coefficient through the reduction in the Reynold's number (16). The low Reynold's number can be directly related to the small size of the airfoil, increase in boundary layer thickness and friction coefficient across the airfoil. It should be noted however that the meanline code assumes the flow is inviscid. This therefore does not allow for the effects of the boundary layer build up.

When looking at a stationary component such as a turbine nozzle, the conditions at the hub and shroud are assumed to be identical. It is in the streamline analysis where radial equilibrium is taken into account.

Table 5: Turbine Stage Meanline Nozzle Exit Pressure and Temperature Conditions

Total Temperature	2222.5	R
Static Temperature	1979.1	R
Total Pressure	37.686	psi
Static Pressure	23.319	psi

### 4.3 Airfoil Generation and Blade Stack-up

Once the meanline is completed there is the need to take this data and generate proper airfoil shapes. Using some help from both Abbott & von Doenhoff (17), as

well as NACA airfoil series data, it was decided that a NACA primary airfoil was to be used. The cascade coordinates were then used in an airfoil profile generation code, which realigned the leading and trailing edge of the blade with the desired flow angles from the meanline code. Then using a simple radial equilibrium calculation, the sets of barrel section airfoils are generated.

After the airfoils are generated, they are placed in an arbitrary location and still require further refinement. There are multiple options available for how a turbine cascade can be stacked: leading edge, trailing edge, or center of gravity. This can vary from design to design, based on the structural limitations imposed on the design. Since the cascade being designed is a turbine nozzle, stacking about the center of gravity was chosen as optimal. The area and centroid of each barrel section is calculated and then each barrel section is moved as necessary to build the stack about the centroid. This in turn provides a turbine cascade which is stacked about the Center of Gravity.

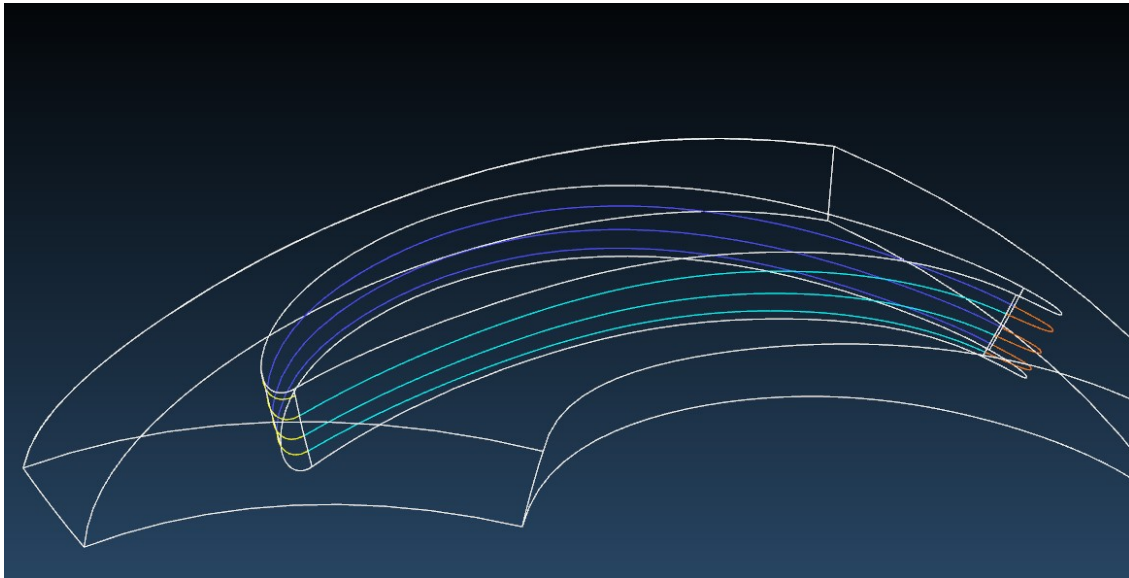


**Figure 17: Barrel Sections of Cascade Stacked about the centroid**

The most critical portion of the design comes in creating the turbine cascade. Noting that if everything performed to this point on paper is done correctly it does not mean a blade will meet its design intent. The generation of the sheets and bodies can make or break the meshing and even the CFD. There are many ways to solve a problem in Unigraphics and more than one fix can lead to a good solution.

#### 4.4 Meshing Geometry and Computational Fluid Dynamics (CFD)

Once the model is built and the geometry is found to be satisfactory by the design engineer, the geometry can be prepped for meshing. This requires the model in the CAD software to be finalized by adding the planes for the inlet, outlet, shroud (if need be) as well as the periodic surfaces, then the model is ready to be moved for meshing and prepped for CFD. For this particular turbine cascade, the ANSYS Workbench was used, Figure 18, which resulted in using the Workbench mesher, also known as ANSYS mesher. The geometry model was imported and the user needs to define the faces, and name them accordingly. The mesh was setup to define a swept type mesh from the shroud to the hub, which left the blade as a bounding wall, this can be shown in Figure 19.

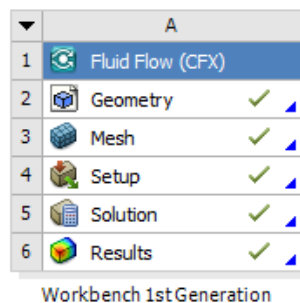
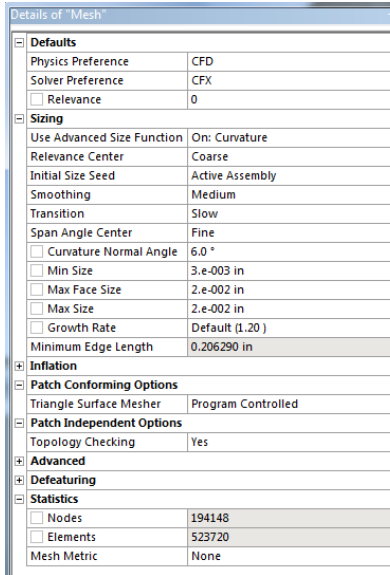
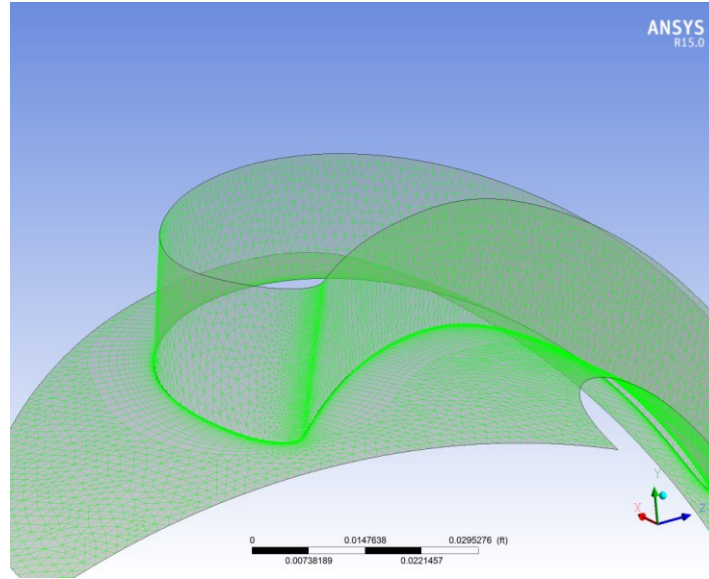


Figure 18: ANSYS Workbench Fluid Flow Project Schematic



**Figure 19: Mesh setup Details Original Turbine Cascade**

The mesh was defined as a Hex dominant mesh and the length parameter was limited to a min size of 0.003” and a max size and max face size of 0.02”, while not allowing the angles to be larger than 6°. The mesh was set to follow the advanced meshing criterion around all curvature. The number of inflation layers was set between 20 and 30 depending on the generation of blade. These aforementioned parameters were varied based on the number of nodes and elements present when the mesh was complete. The goal number was to be in the 100,000-300,000 node range for model fidelity. This number of nodes was determined to be adequate for a first pass. When a final model is defined, the number of elements would be increased. This can be seen in the screenshot showing the hub and blade geometry mesh in Figure 20.



**Figure 20: Swept Mesh of Original Turbine Cascade**

With the mesh found to be of adequate fidelity, the next step is setting up the CFX solver. The conditions for the turbine cascade were pulled from the NPSS model, Table 4 and the inlet condition was set to a total pressure and temperature inlet. The outlet was set to static pressure, which came from the meanline output, Table 5. The blade, shroud and hub were all set as boundary walls for the flow. The surfaces further up and down in the plane of rotation on the Pressure and Suction surface were used as periodic surfaces. The periodic surface allows the creation of a small section and then assumes, based on user input, that there are more surfaces spread over the 360 degree circumference. For this particular case there was the design intent of 9 turbine cascades spread across the 360 degree circumference. Therefore, based upon user inputs, the solver will know that there are 9 cascades equally spaced every 40 degrees. Not only does this periodic input help speed up the time of the solution it also simplifies the input to the model. The next item reviewed was the default domain, where the reference pressures and temperatures were set to 0 and

the fluid type is selected, the heat transfer is set to total energy, and note this is where the solver type is selected. The fluid type used was not that of a standard found in ANSYS. The fluid properties were input via CEF (CFX Expressional Language) and were set to match that used in the solver of NPSS. This enables the designer to maintain the same level of fidelity from start to finish. Now that the parameters are defined for the solver the criterion and time step need to be setup. The criterion was set such that the solver would not stop running until the desired number of iterations is reached, at  $1\text{E}-8$ . The time step was varied but was found to be most accurate around  $1\text{E}-5$ , in the physical time scale setting. For the initial run, the number of iterations were set to 1500.

After all of these parameters were set it was then determined as part of the problem statement to add end wall effects, as if they were coming out of the combustion chamber. These effects do not in any way represent any existing combustor anywhere but were more of an estimate based on the effects of what takes place in the boundary layer. Shown in Figure 21, and Figure 22, is the temperature and pressure gradient, respectively, as a function of span and reflects a decrease of temperature and total pressure at the boundary. These were set as an initial starting point, knowing that during the calculations run inside the solver they would change.

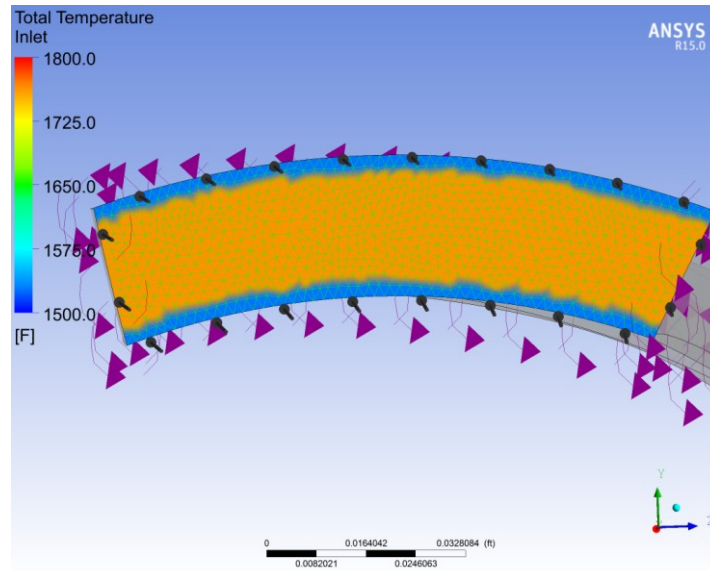


**Figure 21: Total Temperature Inlet Gradient**

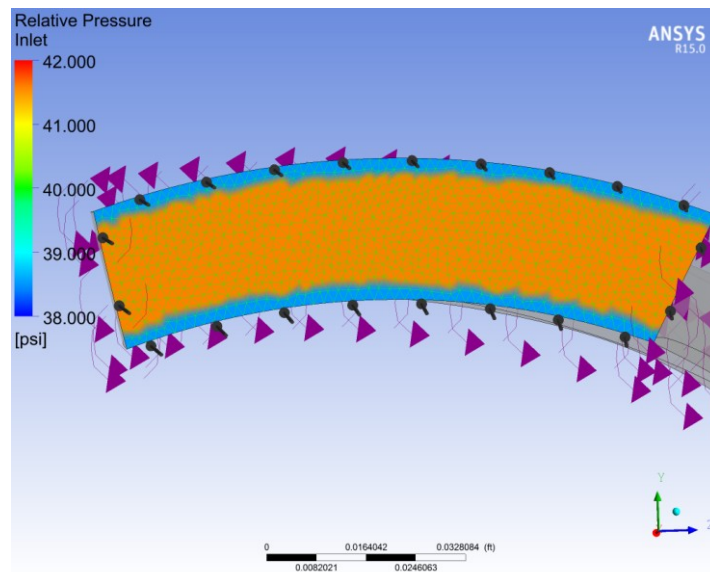


**Figure 22: Total Pressure Inlet Gradient**

The equation setup in CEL was to allow an end wall effect at the hub (0.0 – 0.1 span) and the shroud (0.9 – 1.0 span), Table 6. Without this end wall effect, the flow would be represented as uniform from hub to shroud and would not accurately reflect the problem statement.

**Table 6: CFD Inlet Boundary Gradient Setup**

Boundary Setup	radius < 0.1	0.1 < radius < 0.9	Radius > 0.9	
Inlet Total Pressure	38.5	41.595	38.5	psi
Inlet Total Temperature	1527.3	1762.8	1527.3	F

The solver type was set to a RANS SST (Reynolds-Averaged Navier Stokes Shear Stress Transport) model which is specialized in separation modeling, and this is important for accurate prediction of turbomachinery component performance. An evaluation of available turbulence models was conducted and per a few resources reviewed it was deemed that the SST approach was the most reasonable for airfoil boundary layer applications (18). The CFD model is now formally setup and ready to be run in the CFX solver.

## 5. Results

### 5.1 Comparison of Meanline to CFD

When reviewing the results from the CFD run it is important to have an idea of what is important. For a turbine nozzle it is noted that seeing the normal shockwave at the throat of the cascade is important, because it says the passage is choked which is ideal for a high work turbine stage, Figure 23.

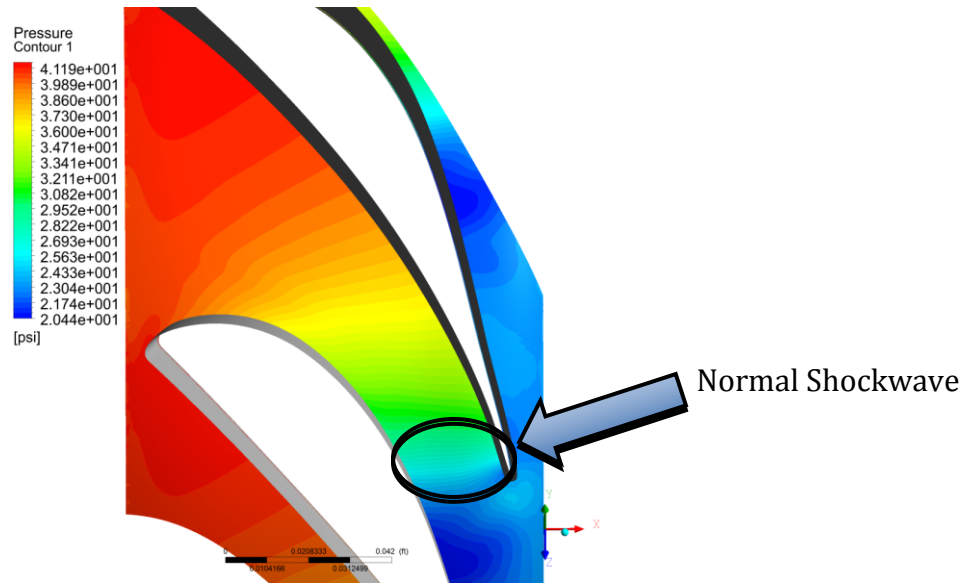


**Figure 23: Meridional View of Static Pressure distribution at 0.5 span**

Reviewing the model in CFX-post, it was deemed to move toward the region of interest to review how the leading edge pressure and temperature stood out against the span, and if indeed the HSV was forming due to the original assumption of inviscid flow. When reviewing the streamlines, Figure 24, it can clearly be seen that there is a region of interest just off of the leading edge of the turbine nozzle Pressure surface.

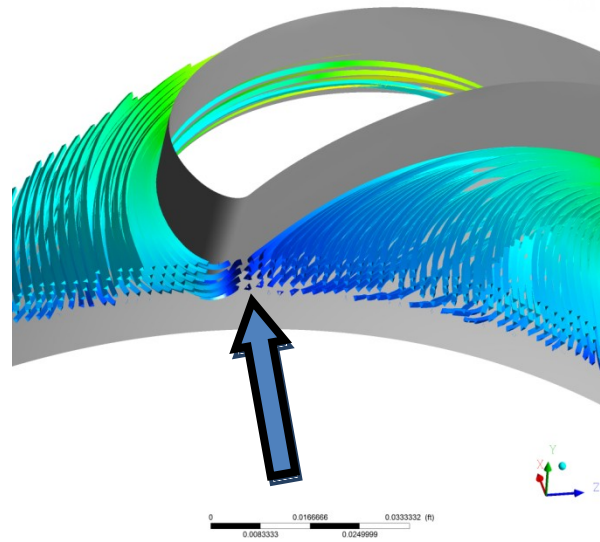


**Figure 24: Velocity streamlines indicating the Saddle Point**

Moving a vector plot in on the constant theta plane and allowing the full blade span to be viewed it can be seen that there is a significant amount of rotation at the lower and upper 20% of the blade span, Figure 25.

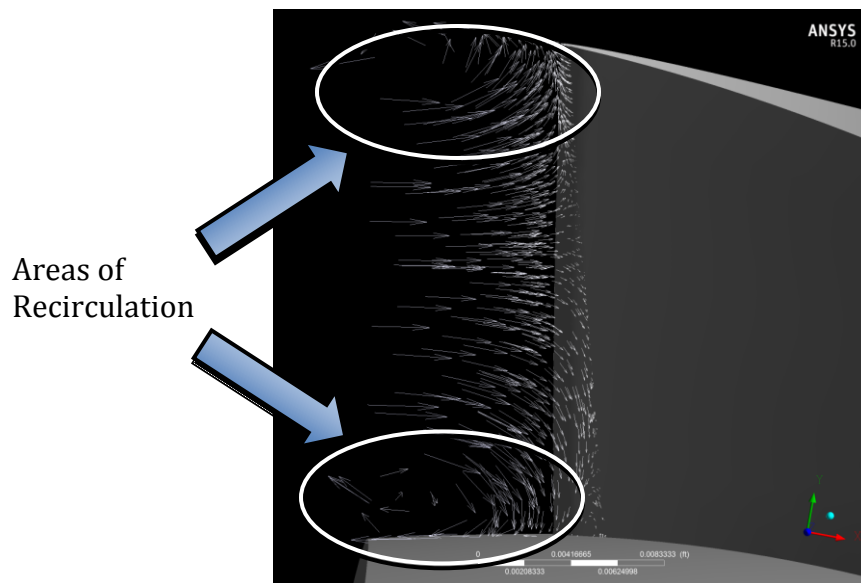


**Figure 25: Velocity Vector plot at the region of interest, full cascade span**

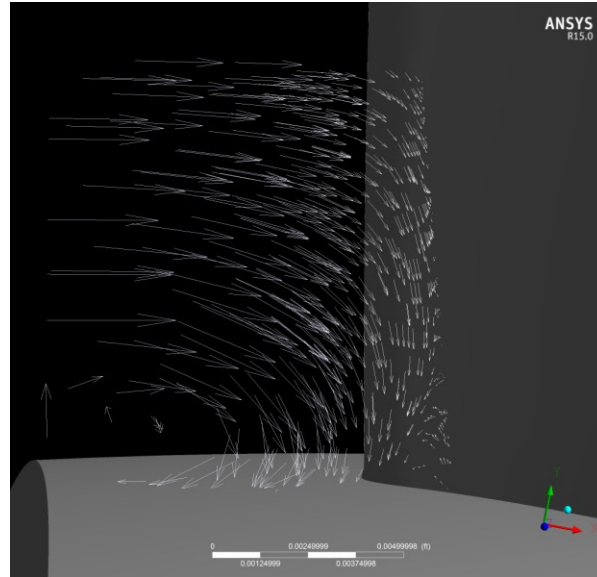


**Figure 26: Velocity vector plot at the region of interest, hub region**

It is evident that the geometry is clearly being affected by the boundary layer, and as the flow stagnates at the saddle point of the cascade it is pushed downward generating a leading edge vortex.

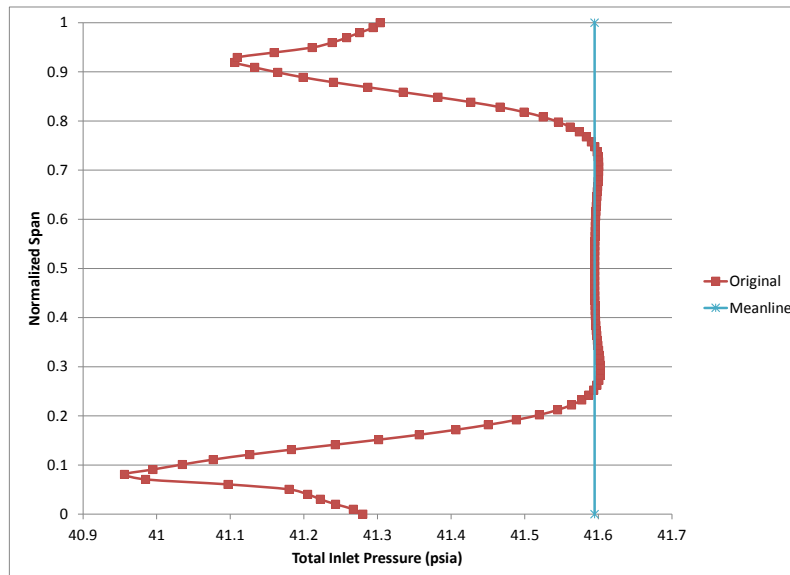


**Figure 27: Comparison of Original CFD Total Pressure distribution to meanline**

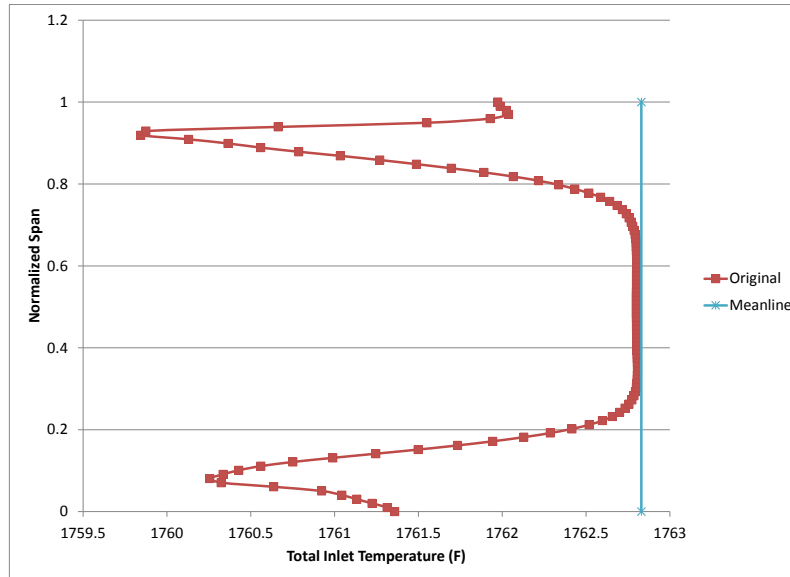


**Figure 28: Comparison of the Original CFD Total Temperature distribution to meanline**

Now that the Horseshoe Vortex has been generated by the variation in flow at the boundary layer the next step is to optimize the airfoil to mitigate the vortex. The method of choice was the approach established by Lethander et al. (14). When discussions took place it was recommended to review some of the methodologies that had been used previously. One approach evaluated was using a fillet where the height to length ratio was 3:1 boundary layers. The results proved to be unfavorable. It was then determined that the key objective is to change the absolute inlet flow angle to help smooth out the inlet axial velocity. By doing this the blade is better optimized for the new, and more realistic, boundary conditions.

## 5.2 Geometry modification for optimization, Original Geometry

In order to find how the geometry was to be manipulated for further optimization the inlet velocity triangles needed to be calculated from the hub to span. This was

done using the axial and circumferential velocities. By doing some basic trigonometry, the absolute flow angle can be calculated, Equation 3.

$$\alpha = \text{atan}\left(\frac{V_{axial}}{V_{circumferential}}\right)$$

**Equation 3: Absolute Flow Angle**

This angle which is optimized using the CFD model will determine how far the hub and shroud geometry need to shift. It is understood that due to the rotation of the flow from the HSV the angle will not be exact at some radial locations between the 0.0 span and the 0.2 span. That leads to the reason of using only the angle at the hub even though it may not be the largest deviation.

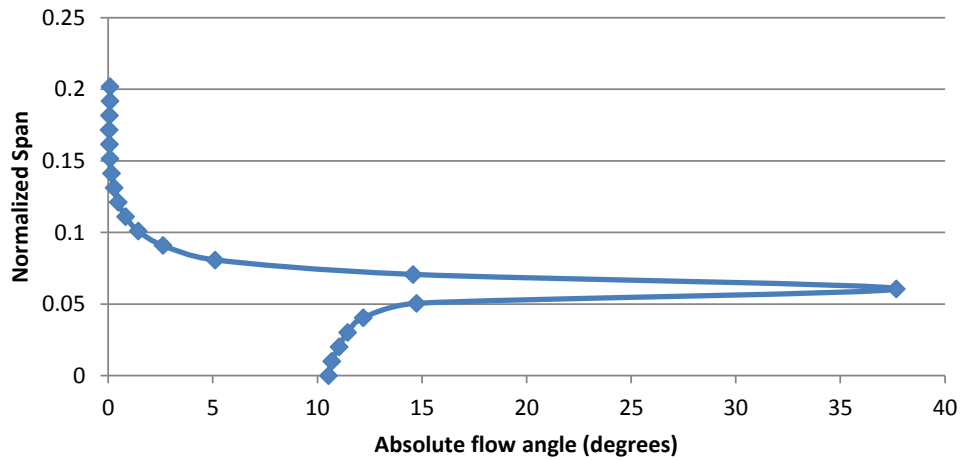


**Figure 29: Absolute Flow angle vs. Normalized Span for Original CFD**

The hub section, is the area of interest, where the cascade geometry needs to be shifted 10 degrees. The reason behind this shift is to change the inlet velocity triangle geometry to create a more uniform axial velocity profile from hub to

shroud. The thought process is that by doing this manipulation the geometry is optimized for the boundary condition.

### 5.2.1 Geometry Optimization

The geometry was manipulated in the CAD model to make the change. Starting with the same CAD model, by turning the hub section then re-sweeping the surface with a variable blend, it would get halfway to the shape needed. After refining the variable blend by adding and removing points the final geometry stack-up was achieved, Figure 30.

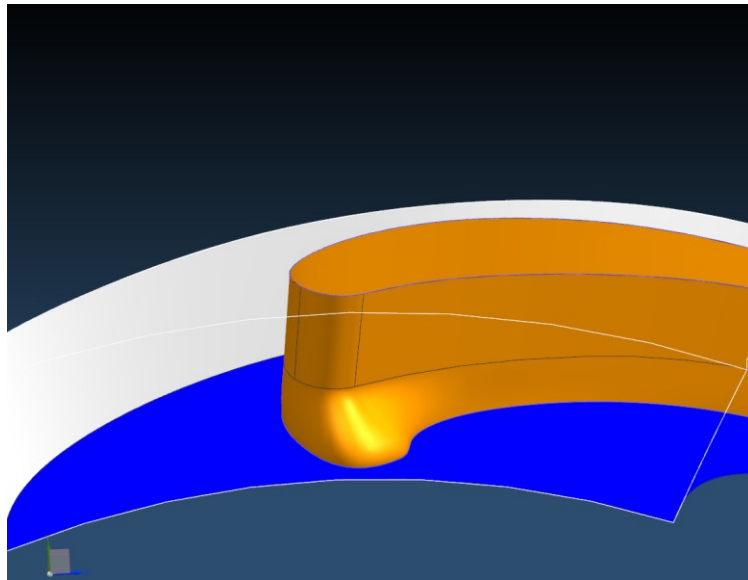


**Figure 30: Optimized Cascade Geometry Stack Up**

It should be noted that the final geometry was not achieved upon on the first trial of optimization, and this was due to the manipulation of the CAD. The appendix shows all other geometry configurations to achieve the desired final optimized design. The mesh methodology was the same as the original blade, yet due to this new “fillet” on the leading edge there would need to be some changes. The Leading edge of the blade was too close to the inlet boundary. The inlet boundary should not be directly

on top of the leading edge of the cascade. If it is, the CFD results can be misleading due to the fact that the flow is not fully developed upon contact with the cascade. This can be fixed by either changing the inlet face generated in the CAD model or by adding a volume ahead of the cascade as it stands. The choice was made to move the face in CAD. The parameters for the CFD mesh did also have to change from their original intent, again this was due to the complex geometry formed. The mesh was still defined as a Hex dominant mesh and the length parameter was limited to a min size of 0.001" and a max size and max face size of 0.03", while not allowing the angles to be larger than 6°. The mesh was set to follow the advanced meshing criterion around all curvature. The number of inflation layers was set between 10 and 20. These measures were taken so that the model would mesh around the complex geometry, but in turn the number of inflation layers had to be reduced in order to not exceed the desired 100,000 – 300,000 nodes.

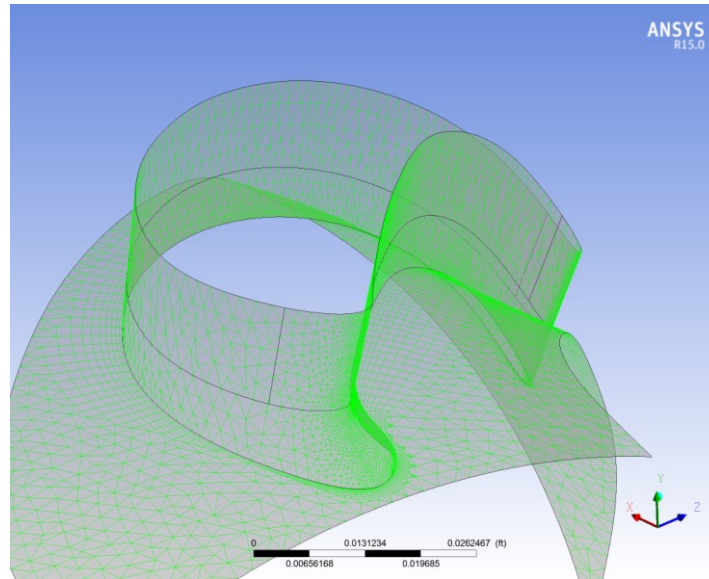


**Figure 31: Final Optimized Geometry showing mesh of Leading edge fillet**

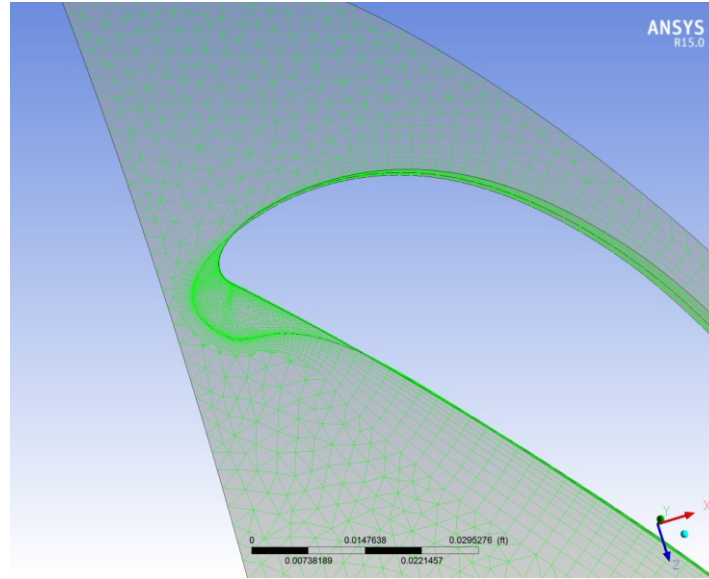


**Figure 32: Top view of mesh for Final Optimized Geometry**

As is shown in Figure 31 and Figure 32 the fineness of the mesh grows drastically around the new leading edge fillet. The CFD solver setup was not changed between any of the CFD runs. The only thing that needed to be done was re-setup the boundary association, but this was mainly taken care of during the mesh process. Upon completion of the CFD run, the leading edge was evaluated. This time the focus was strictly on the formation of the HSV.

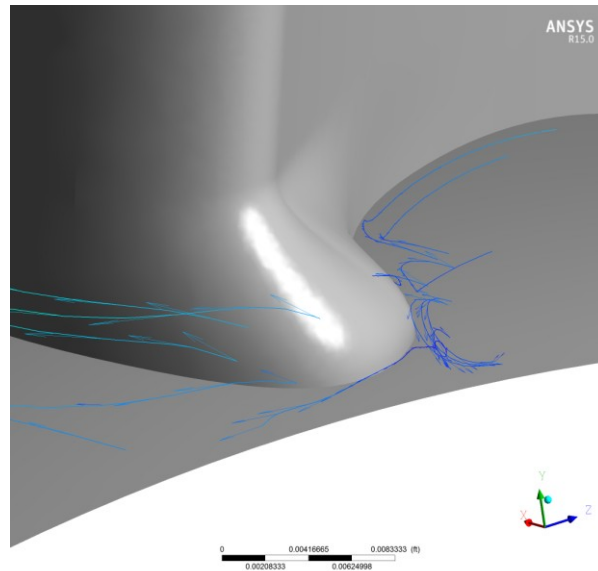


**Figure 33: Optimized Geometry showing HSV with Streamline and Vector plots.**

From the streamline with vector plots in CFX-post it appeared at first that the HSV was still showing, not as strong as before but still here, Figure 33. It was not until diving in a little further that it was noticed that the HSV was indeed not as strong as previously seen, Figure 34.

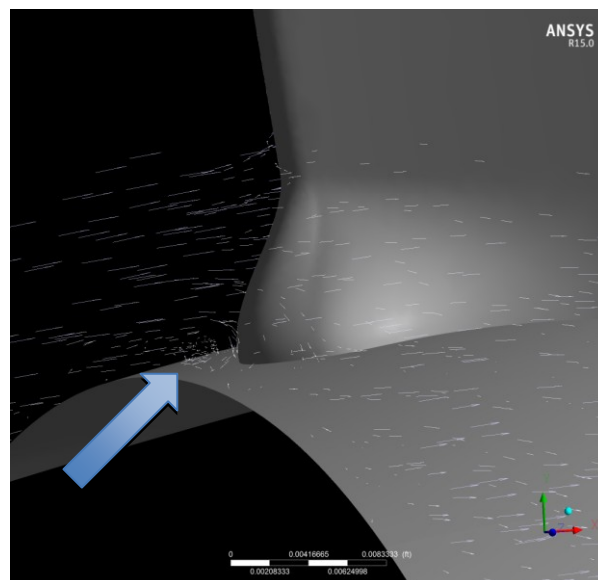


**Figure 34: Optimized Geometry showing weak HSV**

After evaluating the results from Figure 34 there was a need to dive in further to see what exactly was happening. Upon further review of the vector plot in Figure 35, the flow which was generating the vortex in the original model is actually being passed downstream.

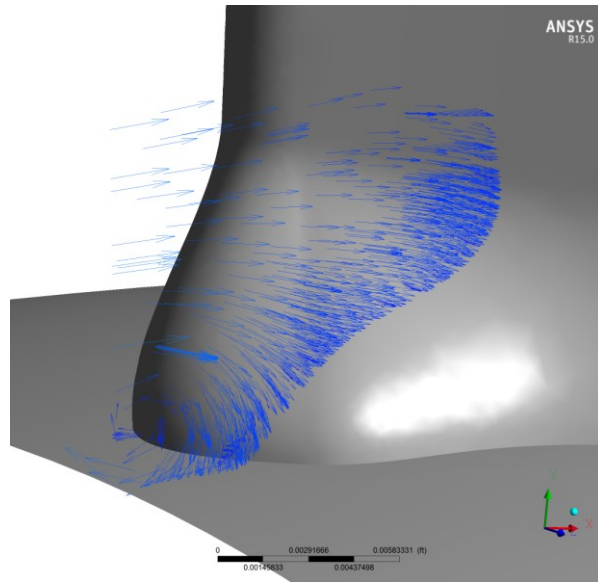


**Figure 35: Optimized Geometry vector plot showing flow moving down passage rather than recirculating**  
There is still some vortex generation at this location where the cascade geometry meets the hub section but this is believed to be formed from how flat and bulbous the leading edge is. This also leads to the thought that by decreasing the radii on the leading edge of the fillet, there can be an even larger improvement.

As the data was reviewed and plotted in Figure 36, Figure 37, and Figure 38, there are a few items of notice. The deviation in Total Pressure from design total pressure is approximately 1%, for static pressure varies by less than 0.5%. The significant factor is the reduction of the temperature in the boundary layer by almost 1.5%. This points to the same conclusion as Lethander et al. (14) that by optimizing the endwall junction of the cascade a reduction in temperature can be seen.

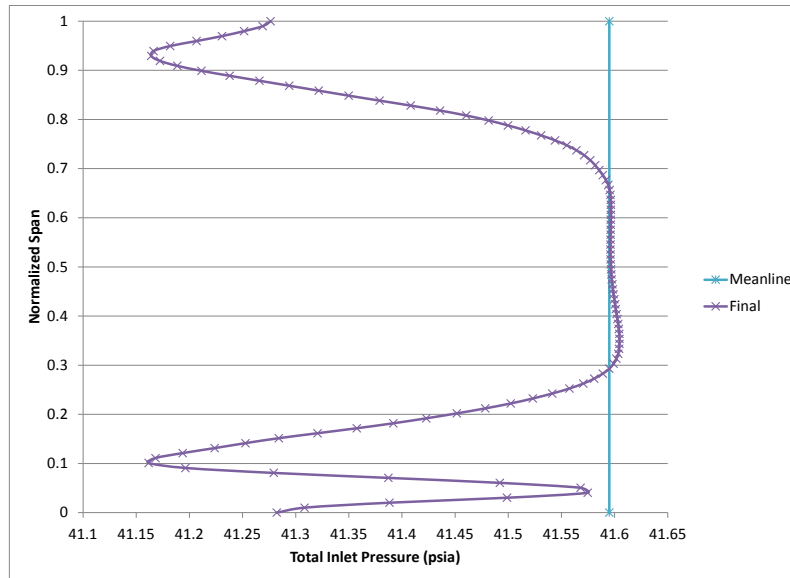


**Figure 36: Inlet Total Pressure vs. Normalized span for Optimized Geometry and Meanline**

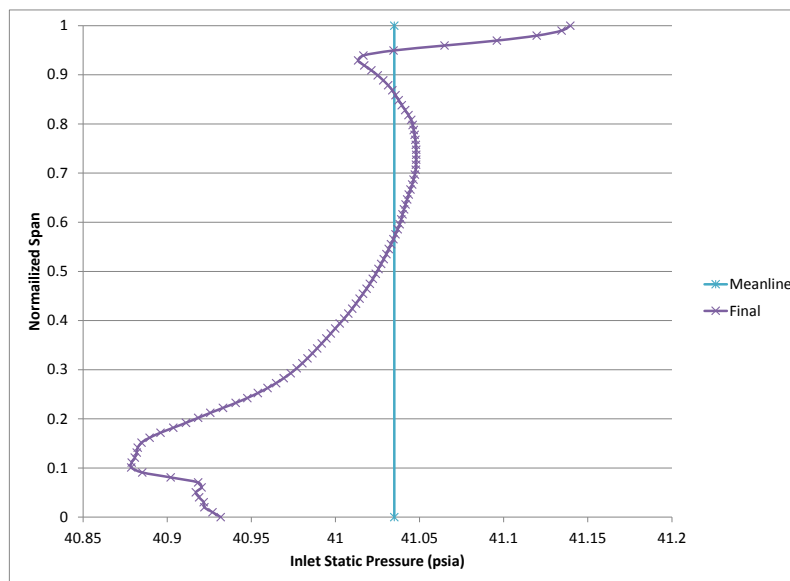


**Figure 37: Inlet Static Pressure vs. Normalized span for Optimized Geometry and Meanline**

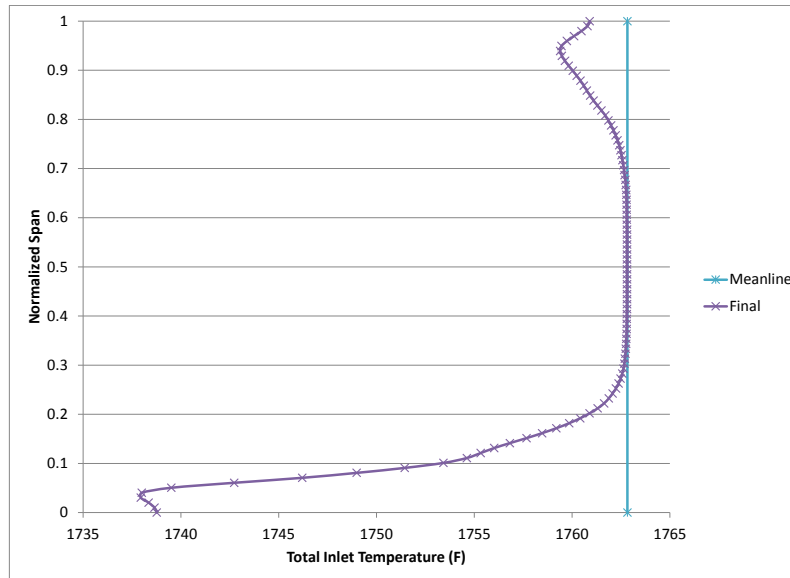


**Figure 38: Inlet Total Temperature vs. Normalized span for Optimized Geometry and Meanline**

## 6. Summary

After reviewing the results from the analyzed geometries it was deemed noteworthy to show the progression from meanline to final design of the Total Pressure and Total Temperature distribution plots. It can be seen that the pressure deviation between the original model and meanline models at the lower twenty percent span has been improved by the geometry optimization, Figure 39, and Figure 40.

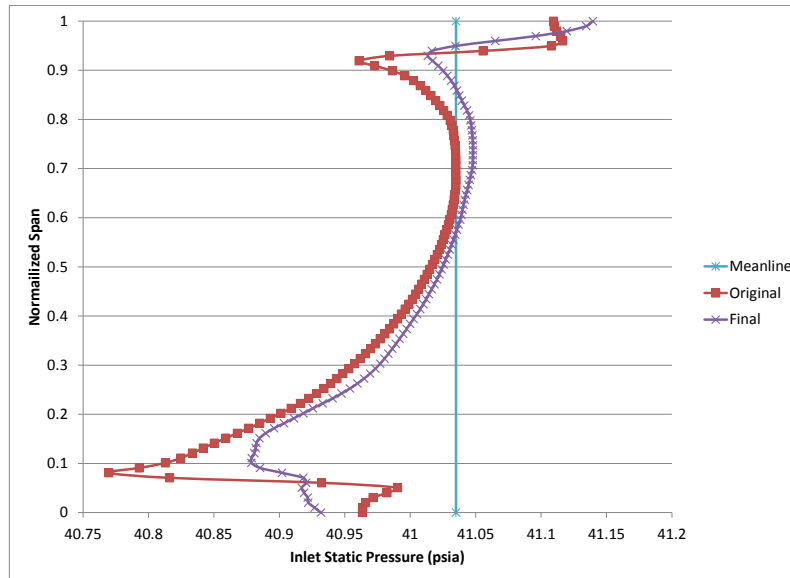


**Figure 39: Inlet Static Pressure vs. Normalized Span for all CFD and Meanline**

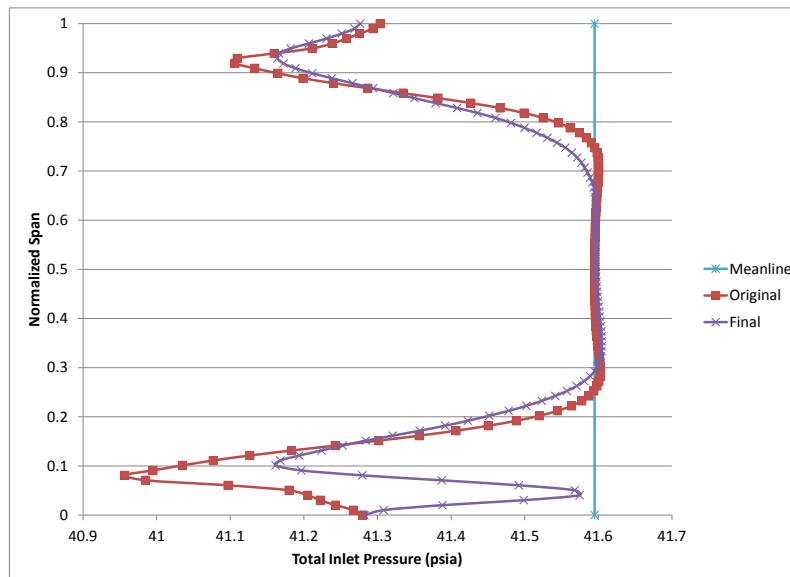


**Figure 40: Inlet Total Pressure vs. Normalized Span for all CFD and Meanline**

When looking at the total temperature plot for the geometries analyzed the total temperature at the hub region is roughly 1.5% colder than the meanline geometry.

This is a byproduct of reducing the endwall effects due to reducing the horseshoe vortex.

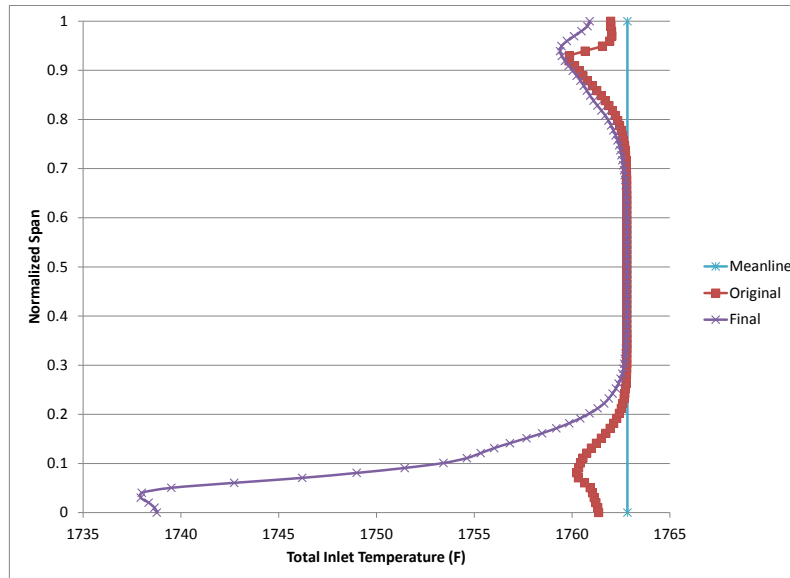


**Figure 41: Inlet Total Temperature vs. Normalized Span for all CFD and Meanline**

The effects of nozzle performance should also be evaluated at the trailing edge where an improvement in span wise total pressure and temperature can be seen, Figure 42 & Figure 43, respectively. There is a 7.58% difference in total pressure at the hub and a 0.12% difference in total temperature, Figure 43.

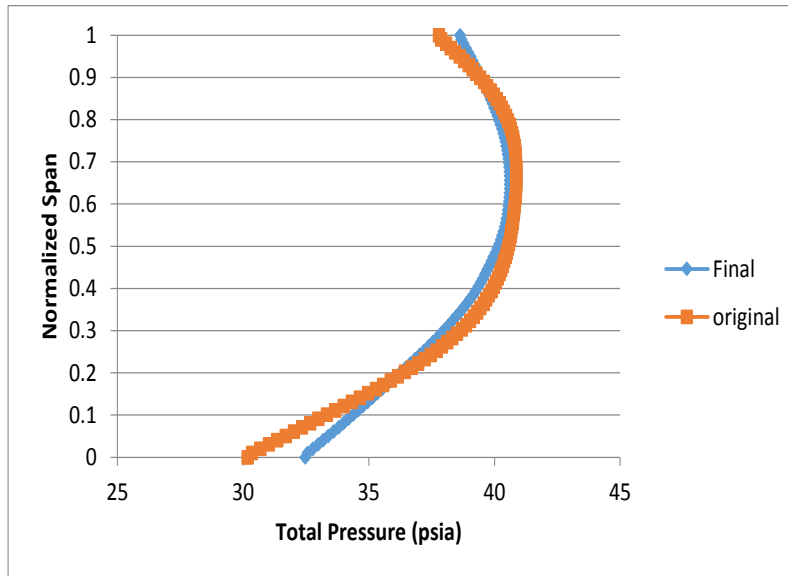


**Figure 42: Exit Total Pressure vs. Normalized Span for CFD**

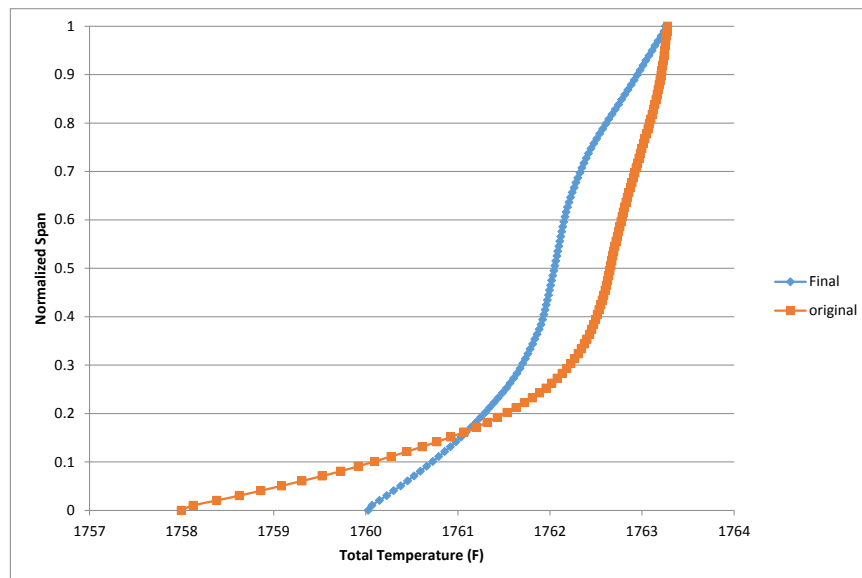


**Figure 43: Exit Total Temperature vs. Normalized Span for CFD**

The preliminary design analysis has been completed and shows the feasibility of a gas turbine for the use in man-portable power generators. This also shows that the horseshoe vortex can be reduced and would improve the overall stage efficiency.

## **7. Future Work / Recommendations**

The future work on this project would be to investigate the effort of the leading edge radius of the fillet has any effect on helping to mitigate the HSV further. This will be followed by the modeling of the rest of the downstream blade rows, where design optimization will need to take place on the nozzle vane cascade to rotor blade interaction. It will also be of interest to see how the turbine rotor performance responds, to the newly designed nozzle vane cascade.

## 8. References

1. "Energy Density." *Wikipedia*. Wikimedia Foundation, 11 Feb. 2014. Web. 05 July 2014. <[http://en.wikipedia.org/wiki/Energy\\_density](http://en.wikipedia.org/wiki/Energy_density)>.
2. "Energizer Technical information." Energizer Technical Information. Energizer, n.d. Web. Nov. 2014. <http://data.energizer.com/PDFs/522.pdf>
3. "EU7000is." Honda EU7000i Model Info. American Honda Motor Co, 2014. Web. Nov. 2014. <http://powerequipment.honda.com/generators/models/eu7000is>
4. "Capstone Turbine Data Sheet." N.p., 2010. Web. Nov. 2014. [http://www.capstoneturbine.com/\\_docs/C30%20Liquid%20Fuel.pdf](http://www.capstoneturbine.com/_docs/C30%20Liquid%20Fuel.pdf)
5. Moran, Michael J., and Howard N. Shapiro. *Fundamentals of Engineering Thermodynamics*. 6th ed. Hoboken: Wiley, 2008. Print.
6. "Turbine Engine Thermodynamic Cycle - Brayton Cycle." *Turbine Engine Thermodynamic Cycle - Brayton Cycle*. Ed. Tom Benson. NASA, 12 June 2014. Web. 04 Aug. 2014. <<http://www.grc.nasa.gov/WWW/k-12/airplane/brayton.html>>.
7. Becker, Frederick E. "Turbomachinery for Man-Portable Military Power Applications." *Http://wstiac.alionscience.com/quarterly* 9.2 (2009): 9-15. *Https://www.dsiac.org/journal/wstiac-quarterly-vol-9-no-2-high-energy-laser-next-generation-ships*. Web. Apr. 2014.
8. "Turbine Design Methodology." Personal interview. Spring 2014.
9. "Textron Lycoming AGT 1500 Turboshaft." *TURBOKART*. N.p., n.d. Web. 05 Oct. 2014. <[http://www.turbokart.com/about\\_agt1500.htm](http://www.turbokart.com/about_agt1500.htm)>.

10. Moustapha, Hany, Mark Zelesky, Nicholas Baines, and David Japikse. *Axial and Radial Turbines*. White River Junction, VT: Concepts NREC, 2003. Print.
11. Kestin, J. *Boundary-layer Theory*. By Hermann Schlichting. 7th ed. New York: McGraw-Hill, 1979. N. pag. Print.
12. Attia, Magdy, Sanjivan Manoharan, Vladislav Shulman, Darrell Stevens, and Laurent Lachmann. "Elimination of the Horse Shoe Vortex in Axial Turbine Vane Cascades via Airfoil Shape Optimization." *AIAA ARC*. AIAA, July 2013. Web. 23 Apr. 2014. <<http://arc.aiaa.org/doi/abs/10.2514/6.2013-3952>>.
13. Zess, G. A., and K. A. Thole. "Computational Design and Experimental Evaluation of Using a Leading Edge Fillet on a Gas Turbine Vane." *Journal of Turbomachinery* 124.2 (2000): 167-75.  
*Http://turbomachinery.asmedigitalcollection.asme.org/article.aspx?articleid=1466369*. ASME, 9 Apr. 2002. Web.
14. Lethander, A. T., K. A. Thole, G. Zess, and Joel Wagner. "Vane-Endwall Junction Optimization to Reduce Turbine Vane Passage Adiabatic Wall Temperatures." *Journal of Propulsion and Power* 20.6 (2004): 1096-104. *No Records*. Web. <<http://arc.aiaa.org/doi/abs/10.2514/1.3887?journalCode=jpp>>.
15. Lethander, A., K. Thole, G. Zess, and Joel Wagner. "Optimizing the Vane-Endwall Junction to Reduce Adiabatic Wall Temperatures in a Turbine Vane Passage." *Proceedings of ASME Turbo Expo 2003* (2003): n. pag.  
*Http://www2.mne.psu.edu/psuexccl/Pubs/2003-Lethander-IGTACE.pdf*. ASME GT2003-38940. Web.

16. Leyes, Richard A., II, and William A. Fleming. *The History of North American Small Gas Turbine Aircraft Engines*. Reston, VA: AIAA, 1999. Print.
17. Abbott, Ira H., and Albert Edward Von. Doenhoff. *Theory of Wing Sections: Including a Summary of Airfoil Data*. New York: Dover, 1959. Print.
18. Eggenpieler, Gilles. *Turbulence Modeling*. Moffett Field, CA: National Aeronautics and Space Administration, Ames Research Center, 1984. *Turbulence Modeling*. ANSYS. Web.  
<[http://www.ansys.com/staticassets/ANSYS/Conference/Confidence/San Jose/Downloads/turbulence-summary-4.pdf](http://www.ansys.com/staticassets/ANSYS/Conference/Confidence/SanJose/Downloads/turbulence-summary-4.pdf)>.

## 9. Appendix A: NPSS model output

Concepts NREC Match - Detail			
Parameter	Design Point	Off-Design Rematch	Units
Altitude	0	0	ft
Mach No.	0	0	
Gross Thrust	0.4081	0.4081	lb <sub>F</sub>
EGT	911.70042	911.70042	R
Net Thrust	0.4081	0.4081	lb <sub>F</sub>
Total Fuel	5.31926	5.31926	lbm
BSFC	0.39666	0.39666	lbm/hr/hp
Thermal Eff	34.86757	34.86757	
Brg Fuel	0	0	lbm/hr
OPR	3.0005	3.0005	
CPR	3.0005	3.0005	
EPR	1.00166	1.00166	
CDP	44.0952	44.0952	psi
CDT	789.96768	789.96768	R
HP Speed	110000	110000	Rpm
Amb.Pt	14.69595	14.69595	psi
Amb.Tt	529.67	529.67	R
Amb.MN	0	0	
Amb.Ps	14.69595	14.69595	R
Amb.Ts	529.67	529.67	psi
Amb.VTAS	0	0	
InFsEng.W	0.18055	0.18055	lbm/s
InEng.Fl_O.W	0.18055	0.18055	lbm/s
InEng.Fl_O.Pt	14.69595	14.69595	psi
InEng.Fl_O.Tt	529.67	529.67	R
InEng.Fl_O.Wc	0.18246	0.18246	lbm/s
InEng.eRam	1	1	
InEng.eRamBase	1	1	
InEng.Fl_O.rhot	0.074892	0.074892	lb/ft <sup>3</sup>
CmpH.Fl_O.W	0.18055	0.18055	lbm/s
CmpH.Fl_O.Pt	44.0952	44.0952	psi
CmpH.Fl_O.Tt	789.96768	789.96768	R
CmpH.Fl_O.Wc	0.074263	0.074263	lbm/s
CmpH.Fl_O.MN	0.4	0.4	
CmpH.Fl_O.Ps	39.51199	39.51194	psi
CmpH.PR	3.0005	3.0005	
CmpH.Nc	108850	108850	Rpm
CmpH.pwr	-16.0452	-16.0452	hp
CmpH.eff	0.746	0.746	
FsEng.LHV	18397	18397	Btu/lbm
FsEng.Fu_O.LHV	18397	18397	Btu/lbm

Parameter	Design Point	Off-Design Rematch	Units
FsEng.Fu_O.switchFuelType	JP	JP	Jet Fuel
FsEng.Fu_O.Pfuel	14.696	14.696	psi
FsEng.Fu_O.Tfuel	540	540	R
FsEng.Fu_O.TrefFuel	0	0	R
FsEng.Fu_O.Wfuel	0.0014776	0.0014776	lbm/s
FsEng.Wfuel	0	0	lbm/s
BrnPri.Fl_I.W	0.18055	0.18055	lbm/s
BrnPri.Fl_I.Pt	43.0952	43.0952	psi
BrnPri.Fl_I.Tt	1712.65411	1712.65411	R
BrnPri.Fl_I.Wc	0.11188	0.11188	lbm/s
BrnPri.Fl_O.W	0.18203	0.18203	lbm/s
BrnPri.Fl_O.Pt	41.5952	41.5952	psi
BrnPri.Fl_O.Tt	2222.47789	2222.47789	R
BrnPri.Fl_O.Wc	0.13313	0.13313	lbm/s
BrnPri.TtCombOut	2222.5	2222.5	R
BrnPri.Wfuel	0.0014776	0.0014776	lbm/s
BrnPri.FAR	0.0081835	0.0081835	
BrnPri.eff	0.998	0.998	
B041.Fl_I.W	0.18203	0.18203	lbm/s
B041.Fl_I.Pt	41.5952	41.5952	psi
B041.Fl_I.Tt	2222.47789	2222.47789	R
B041.Fl_I.Wc	0.13313	0.13313	lbm/s
B041.Fl_I.MN	0	0	
B041.Fl_I.Ps	0	0	
B041.Fl_I.FAR	0.0081835	0.0081835	
B041.Fl_O.W	0.18203	0.18203	lbm/s
B041.Fl_O.Pt	41.5952	41.5952	psi
B041.Fl_O.Tt	2222.47789	2222.47789	R
B041.Fl_O.Wc	0.13313	0.13313	lbm/s
B041.Fl_O.MN	0	0	
B041.Fl_O.FAR	0.0081835	0.0081835	
TrbH.Fl_O.W	0.18203	0.18203	lbm/s
TrbH.Fl_O.Pt	15.72043	15.72043	psi
TrbH.Fl_O.Tt	1815.179	1815.179	R
TrbH.Fl_O.Wc	0.31834	0.31834	lbm/s
TrbH.eff	0.87	0.87	
TrbH.pwrExpand	29.60322	29.60322	hp
Perf.TrbH_DHRC	27.55136	27.55136	Btu/hr
TrbH.PR	2.64593	2.64593	

Parameter	Design Point	Off-Design Rematch	Units
HX.effect	0.9	0.9	BTU/s
HX.Q	-42.73504	-42.73504	lbm/s
HX.FI_I1.Wc	0.074263	0.074263	lbm/s
HX.FI_I1.W	0.18055	0.18055	psi
HX.FI_I1.Pt	44.0952	44.0952	R
HX.FI_I1.Tt	789.96768	789.96768	lbm/s
HX.FI_I2.Wc	0.31834	0.31834	lbm/s
HX.FI_I2.W	0.18203	0.18203	psi
HX.FI_I2.Pt	15.72041	15.72041	R
HX.FI_I2.Tt	1815.17482	1815.17482	lbm/s
HX.FI_O1.Wc	0.11188	0.11188	lbm/s
HX.FI_O1.W	0.18055	0.18055	psi
HX.FI_O1.Pt	43.0952	43.0952	R
HX.FI_O1.Tt	1712.65411	1712.65411	lbm/s
HX.FI_O2.Wc	0.24094	0.24094	lbm/s
HX.FI_O2.W	0.18203	0.18203	psi
HX.FI_O2.Pt	14.72041	14.72041	R
HX.FI_O2.Tt	911.70042	911.70042	
Perf.HotDelta	1	1	
Perf.ColdDelta	1	1	
Pressure drop	2	2	lbm/s
B042.FI_I.W	0.18203	0.18203	psi
B042.FI_I.Pt	14.72041	14.72041	R
B042.FI_I.Tt	911.70042	911.70042	lbm/s
B042.FI_I.Wc	0.24094	0.24094	
B042.FI_I.MN	0	0	lbm/s
B042.FI_O.W	0.18203	0.18203	psi
B042.FI_O.Pt	14.72041	14.72041	R
B042.FI_O.Tt	911.70042	911.70042	lbm/s
B042.FI_O.Wc	0.24094	0.24094	lbm/s
D060.FI_O.W	0.18203	0.18203	psi
D060.FI_O.Pt	14.72041	14.72041	R
D060.FI_O.Tt	911.70042	911.70042	lbm/s
D060.FI_O.Wc	0.24094	0.24094	psi
D060.FI_O.Ps	13.19619	13.19615	
D060.FI_O.MN	0.4	0.4	ft/s
D060.FI_O.V	580.45239	580.4537	
D060.FI_O.FAR	0	0	lbm/s
NozPri.FI_O.W	0.18203	0.18203	

Parameter	Design Point	Off-Design Rematch	Units
NozPri.Fl_O.Pt	14.72041	14.72041	psi
NozPri.Fl_O.Tt	911.70042	911.70042	R
NozPri.Fl_O.Wc	0.24094	0.24094	lbm/s
NozPri.Fl_O.Ps	14.69595	14.69595	psi
NozPri.Fl_O.Ts	911.27828	911.27828	R
NozPri.PR	1.00166	1.00166	
NozPri.Fl_O.V	72.13082	72.13082	ft/s
NozPri.AR	1	1	
NozPri.Ag	8.34826	8.34826	in <sup>2</sup>
NozPri.Af	8.34826	8.34826	in <sup>3</sup>
NozPri.Fl_O.Aphy	8.34826	8.34826	in <sup>4</sup>
NozPri.Cv	1	1	
NozPri.Cd	1	1	
NozPri.Cfg	1	1	
NozPri.Fl_O.MN	0.048993	0.048993	
NozPri.Fg	0.4081	0.4081	lb <sub>F</sub>
NozPri.FgIdeal	0.4081	0.4081	lb <sub>F</sub>
ShH.Nmech	110000	110000	Rpm
ShH.pwrOut	-29.4552	-29.4552	hp
ShH.trqIn	1.41345	1.41345	ft*lb <sub>F</sub>
ShH.trqNet	-1.4877E-14	-1.4877E-14	ft*lb <sub>F</sub>
ShH.bearingFuelFlow	0	0	lbm/s
Load16.pwr	-13.41	-13.41	hp
Load16.Nload	110000	110000	Rpm
Load16.NR	1	1	
Load16.trqLoad	-0.64028	-0.64028	ft*lb <sub>F</sub>
Load16.trq	-0.64028	-0.64028	ft*lb <sub>F</sub>